Radiation Hydrodynamics of Turbulent H II Regions in Molecular Clouds: A Physical Origin of LyC Leakage and the Associated Lyα Spectra

Koki Kakiichi[1] and Max Gronke[2,3]
[1] Department of Physics and Astronomy, University College London, UK; k.kakiichi@ucl.ac.uk
[2] Department of Physics and Astronomy, University of California, Santa Barbara, CA, USA

Abstract

We examine Lyman continuum (LyC) leakage through H II regions regulated by turbulence and radiative feedback in a giant molecular cloud in the context of fully coupled radiation hydrodynamics (RHD). The physical relations of the LyC escape with H I covering fraction, kinematics, ionizing photon production efficiency, and emergent Lyα line profiles are studied using a series of RHD turbulence simulations performed with RAMSES-RT. The turbulence-regulated mechanism allows ionizing photons to leak out at early times before the onset of supernova feedback. The LyC photons escape through turbulence-generated low column density channels that are evacuated efficiently by radiative feedback via photoheating-induced shocks across the D-type ionization fronts. The Lyα photons funnel through the photoionized channels along the paths of LyC escape, resulting in a diverse Lyα spectral morphology including narrow double-peaked profiles. The Lyα peak separation is controlled by the residual H I column density of the channels, and the line asymmetry correlates with the porosity and multiphase structure of the H II region. This mechanism through the turbulent H II regions can naturally reproduce the observed Lyα spectral characteristics of some of the LyC-leaking galaxies. This RHD turbulence origin provides an appealing hypothesis to explain high LyC leakage from very young (∼3 Myr) star-forming galaxies found in the local universe without need of extreme galactic outflows or supernova feedback. We discuss the implications of the turbulent H II regions on other nebular emission lines and a possible observational test with the Magellanic System and local blue compact dwarf galaxies as analogs of reionization-era systems.

1. Introduction

Understanding the physical origin of ionizing radiation escape through the interstellar medium (ISM) of star-forming galaxies is critical to understanding the sources of reionization. For galaxies to drive H I reionization, the escape fraction of Lyman continuum (LyC) photons, f_{esc}^{LyC}, must be as large as ∼10%–20% at $6 \lesssim z \lesssim 12$ (e.g., Robertson et al. 2015) to be consistent with the UV luminosity function (Bouwens et al. 2015; Oesch et al. 2018) and the measure of the Thomson optical depth to the cosmic microwave background (Planck Collaboration et al. 2020). At the tail end of reionization, galaxies are thought to drive the large-scale UV background fluctuation in the intergalactic medium (Becker et al. 2018), and the indirect measure suggests a probable increase of the average escape fraction to $\gtrsim 8\%$ at $z \gtrsim 5$–6 (Kakiichi et al. 2018; Meyer et al. 2019). However, little is known about the physical origin of ionizing escape or the cause of the required rise in the ionizing power of galaxies toward the reionization epoch.

Recent deep Hubble Space Telescope (HST) imaging campaigns (Siana et al. 2015; Fletcher et al. 2019; Oesch et al. 2018) and ground-based deep spectroscopic searches (Marchi et al. 2017; Steidel et al. 2018) have revealed a signature of the LyC leakages along the lines of sight of Lyα emitters (LAEs) and Lyman-break galaxies (LBGs), providing a valuable sample with which the origin of LyC escape can be directly studied. These $z \sim 2$–3 LyC-leaking LAEs are young and associated with intense [O III] emission, which suggests a spectrally hard stellar population with low metallicity resembling star-forming systems at $6 < z < 12$

(Nakajima et al. 2016). Further details are provided by the Cosmic Origin Spectrograph (COS) on board HST, which has revealed LyC detection from low-redshift dwarf galaxies with high [O III]/[O II] line ratios (Izotov et al. 2016, 2018b). Complementary Lyα and UV-to-optical spectroscopy and spatially resolved images of low-redshift LAE analogs (Hayes et al. 2014; Jaskot & Oey 2014; Östlin et al. 2014; Henry et al. 2015) make it possible to examine the inner working of these similar classes of LyC-leaking systems.

For triggering the leakage of ionizing radiation, a commonly held view is that stellar feedback such as supernova explosions drives galactic outflows, creating low column density channels in the ISM through which LyC photons escape (e.g., Kimm & Cen 2014; Wise et al. 2014). Observationally, however, while outflows are ubiquitous in LyC-leaking galaxies and some with an extreme value (Heckman et al. 2011; Borthakur et al. 2014), their outflow kinematics may not be statistically different from non-LyC-leaking systems (Chisholm et al. 2017; Jaskot et al. 2017). Also, the presence of prominent P Cygni O IV $\lambda 1035$ and N V $\lambda 1240$ profiles from massive stars, which arise from stellar winds, suggests very young ages (∼2–3 Myr) for local LyC-leaking galaxies (Izotov et al. 2018b), indicating that there is little time for supernova explosions to expel gas from the birth cloud. The H I absorption spectra in the gamma-ray burst afterglow, which traces the direct environment of star-forming regions and the ISM at the death of a massive star (Prochaska et al. 2006; Vreeswijk et al. 2013), reveals ubiquitous optically thick gas and a high H I covering fraction, indicating a low LyC escape fraction of <1.5% (Chen et al. 2007; Fynbo et al. 2009; Tanvir et al. 2019). These seem to challenge the picture that supernova and galactic outflows solely trigger the LyC leakage. Clearly, the physics is far from simple, and the observational diversity requires that any successful

---
[3] Hubble Fellow.

theory of escape fraction should be able to explain not only why the escape fraction can be high but also the diversity of LyC escape fractions.

To this end, we wish to examine other mechanisms of LyC leakage invoking turbulence and H II region feedback that can operate at an early time of the star-forming clouds before supernova explosions occur. The formation and evolution of the H II region in a turbulent molecular cloud is a natural consequence of the gravoturbulent fragmentation paradigm of star formation (e.g., Krumholz & McKee 2005; Federrath & Klessen 2012), which has been subject to many theoretical studies (Krumholz et al. 2006, 2012; Mellema et al. 2006; Arthur et al. 2011; Dale et al. 2012; Kim et al. 2016, 2018). Recent high-resolution, cosmological galaxy formation simulations suggest that the small 10–100 pc-scale environment around star-forming regions is likely the key process in regulating the leakage of ionizing radiation (Kimm & Cen 2014; Paardekooper et al. 2015; Trebitsch et al. 2017). The galaxies experience substantial LyC leakage when the optically thick gas is evacuated from the parsec-scale environment of massive stars during the period when the stars still can provide abundant ionizing photons (Ma et al. 2015, 2016). The spatial scale required for understanding LyC leakage is indeed approaching that of giant molecular clouds (GMCs).

For any given scenario of LyC leakage, it is critical to understand the connection between the LyC escape fraction and other spectroscopic features, including Lyα and the [O III]/[O II] line ratio. This is important as a test of a theory. Also, because the direct LyC leakage from the $6 < z < 12$ galaxies at the heart of the reionization era cannot be observed, even with the James Webb Space Telescope (JWST), any inference on their ionizing capabilities must rely on an interpretation of other observable rest-UV or optical signatures, such as nebular emission (Inoue 2011; Zackrisson et al. 2013, 2017; Tamura et al. 2019) and UV absorption lines (Jones et al. 2013; Leethochawalit et al. 2016; Chisholm et al. 2018; Gazagnes et al. 2018).

Because its unique brightness and omnipresence throughout cosmic time allow us to observe it in a large sample of galaxies (e.g., Ouchi et al. 2018; Wisotzki et al. 2018), Lyα is particularly important. In addition, Lyα is a resonant line of neutral hydrogen with a cross section at the line center approximately 3 orders of magnitude larger than that of LyC photons connecting Lyα escape processes to LyC ones. Furthermore, since each interaction between an H I atom and a Lyα photon shifts the photon's frequency, the emergent Lyα spectral shape is indicative of the system's neutral hydrogen distribution and kinematics. All of these factors make Lyα observables important diagnostics to be correlated with LyC escape. This natural "Lyα–LyC" connection has been explored in several theoretical studies (e.g., Verhamme et al. 2015; Dijkstra et al. 2016b), and recently, the correlation between the Lyα and LyC escape fraction, as well as other Lyα line properties, e.g., peak separation, has been observationally studied (Verhamme et al. 2017; Izotov et al. 2018b; Marchi et al. 2018; Steidel et al. 2018).

However, thus far, these Lyα–LyC studies have relied on either simplified models of gas and kinematics, e.g., a shell or clumpy medium (Verhamme et al. 2015; Dijkstra et al. 2016b), or postprocessing of cosmological galaxy formation simulations (Yajima et al. 2014). Although there has been substantial progress in both cosmological (e.g., Pawlik et al. 2015, 2017; Gnedin 2016; Rosdahl et al. 2018) and zoom-in simulations for understanding the origin of Lyα (Smith et al. 2019), as well as nebular and infrared lines (Katz et al. 2019), resolving the subparsec structures in H II regions, GMCs, and the cold gas phase in general, including the circumgalactic medium (CGM; e.g., van de Voort et al. 2019; Hummels et al. 2019), still remains difficult. A study of the connection between LyC escape and Lyα transfer using the detailed radiation hydro-dynamic (RHD) simulations of individual H II regions and GMCs (Geen et al. 2015, 2016; Howard et al. 2017, 2018; Kim et al. 2018) has not yet been carried out (except for Kimm et al. 2019, upon completion of this work). In this paper, we examine the LyC leakage mechanism and emergent Lyα line profiles using a series of RHD turbulence simulations representing a patch of an H II region in a GMC. Using the controlled local simulations, we analyze the process responsible for the Lyα–LyC connection and the relation to turbulence kinematics, radiative feedback, and ionizing photon production efficiency. Our goal is to understand the origin of the Lyα–LyC connection found in the observed LyC-leaking sample, as well as to provide a benchmark for future global simulations of molecular clouds and galaxies.

The paper is organized as follows. Section 2 introduces the various regimes of LyC leakage. The numerical simulations and setup are described in Section 3. We present the results of the LyC leakage mechanism through the turbulent H II regions in Section 4, followed by the connection with the emergent Lyα line profiles in Section 5. We discuss the limitation of our simulations and possible observational tests in Section 6. The conclusion is summarized in Section 7.

2. LyC Leakage Mechanism

In the simple commonly held picture (Zackrisson et al. 2013; Reddy et al. 2016; Steidel et al. 2018), LyC leakage is leveraged by (i) the ionization-bound nebulae with holes or (ii) density-bound nebulae. The escape fractions in the two regimes are as follows.

Ionization-bound LyC leakage. In this scenario, the LyC photons escape through holes of low column density channels through the ISM, but in the other directions, the ionization front (I-front) is bound within the nebula (i.e., ionization-bound). Thus, the escape fraction is determined by the availability of the holes through the ISM,

$$f_{\rm esc}^{\rm LyC}(\text{ionization-bound}) \sim 1 - f_{\rm cov}, \qquad (1)$$

where $f_{\rm cov}$ is the fraction of lines of sight around ionizing sources (e.g., massive stars) covered by the optically thick gas. Such holes can be created by turbulence or stellar feedback, including photoionization, radiation pressure, stellar winds, and supernovae.

Density-bound LyC leakage. In this scenario, the intense radiation from massive stars ionizes all the gas in the ISM; thus, the I-front is no longer bound inside the system (i.e., density-bound). This allows LyC photons to brute-forcefully escape out of the system by ionizing all the gas along the way. Thus, the escape fraction is given by the fraction of photons that have not been absorbed in the ISM (Dove & Shull 1994; Benson et al. 2013),

$$f_{\rm esc}^{\rm LyC}(\text{density-bound}) \sim 1 - \frac{\dot{N}_{\rm rec}}{\dot{N}_{\rm ion}}, \qquad (2)$$

where $\dot{N}_{\rm rec}$ is the recombination rate and $\dot{N}_{\rm ion}$ is the LyC photon production rate of the star-forming regions.
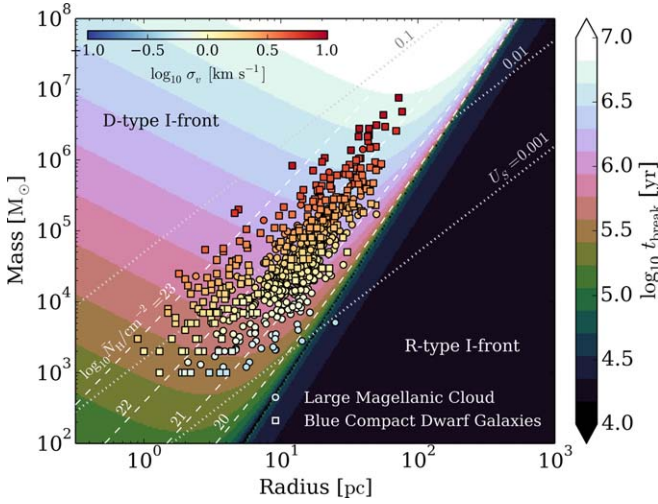
Figure 1. The filled contours show the time required for the I-front to break out of a GMC, t_{break}, at a given mass and radius assuming a spherical uniform cloud. The circles and squares denote the observed mass, radius, and velocity dispersion of GMCs in the LMC (Wong et al. 2011) and blue compact dwarf galaxies (Kepley et al. 2016; Imara & Faesi 2018; Miura et al. 2018), which are overlaid to guide a relevant parameter space. The dashed lines indicate the total gas column density of the shell between the initial Strömgren radius R_S and cloud radius R_{cl}, and the dotted lines indicate the ionization parameter at the Strömgren radius. The figure illustrates that the I-fronts in the majority of GMCs are likely the D-type.

In reality, an individual H II region will consist of both ionization- and density-bound directions, and a galaxy consists of an ensemble of H II regions. This highlights the two important factors in controlling LyC escape: (i) the modes of creating low column density channels, e.g., by turbulence or radiative and/or stellar feedback, through which I-fronts can break out of a natal star-forming cloud, and (ii) the large LyC production rate of star-forming regions to compensate for the recombination rate in the density-bound photoionized channels.

2.1. Nature of I-fronts: H II Regions in Turbulent Molecular Clouds

In the gravoturbulent fragmentation paradigm (e.g., Krumholz & McKee 2005; Federrath & Klessen 2012), stars form in dense clumps generated by the supersonic turbulence in a GMC, providing a low star formation efficiency $\epsilon_\star$ (a few to several percent; e.g., McKee & Ostriker 2007; Kennicutt & Evans 2012) —defined as the fraction of a cloud's gas mass that is converted into stars—and kinetic support against gravitational collapse. In Figure 1, we show the observed mass, size, and turbulent velocity dispersion of GMCs in the Large Magellanic Cloud (LMC; Wong et al. 2011) and blue compact dwarf galaxies (II Zw 40, Kepley et al. 2016; NGC 5253, Miura et al. 2018; Henize 2–10, Imara & Faesi 2018) that share similar properties to those observed at high redshift (Izotov et al. 2011; Crowther et al. 2017). Although the properties of molecular clouds in LyC-leaking systems and high-redshift galaxies are unknown, GMCs in the environments of nearby dwarfs serve as a guideline for the relevant parameter space.

To identify the LyC leakage mechanism, let us consider a spherical homogeneous cloud of gas mass M_{cl} and radius R_{cl} with a central source of stellar mass $M_\star = \epsilon_\star M_{\mathrm{cl}}$ with an ionizing photon production rate (in units of photons per second),

$$\dot{N}_{\mathrm{ion}} = \xi_{\mathrm{ion}} \epsilon_\star M_{\mathrm{cl}}$$

$$\simeq 1.9 \times 10^{50} \left(\frac{\epsilon_\star}{0.05}\right)\left(\frac{M_{\mathrm{cl}}}{10^5 M_\odot}\right) \mathrm{s}^{-1}. \qquad (3)$$

A single stellar population of 1 Myr after starburst with stellar metallicity $Z_\star = 0.002$ from the binary stellar population code BPASS (BPASSV2.1_IMF135_100; Eldridge et al. 2017) yields the ionizing photon production rate per stellar mass of $\xi_{\mathrm{ion}} = 3.8 \times 10^{46}$ photons $\mathrm{s}^{-1} M_\odot^{-1}$. The corresponding Strömgren radius is

$$R_S = \left(\frac{3 \dot{N}_{\mathrm{ion}}}{4\pi a_B \bar{n}_0^2}\right)^{1/3}$$

$$\simeq 7.4 \left(\frac{\epsilon_\star}{0.05} \frac{M_{\mathrm{cl}}}{10^5 M_\odot}\right)^{1/3} \left(\frac{R_{\mathrm{cl}}}{20\mathrm{pc}}\right)^2 \mathrm{pc}, \qquad (4)$$

where $\alpha_B \approx 2.6 \times 10^{-13} T_4^{-0.7}$ cm^3 s^{-1} ($T_4 = T/10^4$ K) is the case B recombination rate and $\bar{n}_0 \simeq 120.8 \times (M_{\mathrm{cl}}/10^5 M_\odot)$ $(R_{\mathrm{cl}}/20 \, \mathrm{pc})^{-3}$ cm^{-3} is the mean number density of hydrogen nuclei. The dimensionless ratio of the cloud radius to the Strömgren radius sets whether the H II region can break out of the cloud during its early phase of rapid expansion (known as R-type). If $R_{\mathrm{cl}} < R_S$, the R-type I-front radius expands as $r_I(t) = R_S(1 - e^{-t/t_{\mathrm{rec}}})^{1/3}$ (e.g., Shu 1992) and rapidly approaches the Strömgren radius in order of recombination timescale $t_{\mathrm{rec}} = (\alpha_B \bar{n}_0)^{-1} \approx 1.2 T_4^{0.7} (\bar{n}_0/100 \, \mathrm{cm}^{-3})^{-1}$ kyr. The R-type I-front therefore breaks out of the parent cloud, $r_I(t_{\mathrm{break}}) = R_{\mathrm{cl}}$, after

$$t_{\mathrm{break}} = t_{\mathrm{rec}} \ln \left[1 - \left(\frac{R_{\mathrm{cl}}}{R_S}\right)^3\right]^{-1} \text{ for R-type I-front.} \qquad (5)$$

The LyC leakage immediately follows the density-bound regime. Using Equation (2), we find

$$f_{\mathrm{esc}}^{\mathrm{LyC}} = 1 - \frac{\alpha_B \bar{n}_0}{m_H \epsilon_\star \xi_{\mathrm{ion}}} \text{ after R-type breakout.} \qquad (6)$$

The density-bound LyC leakage following the early R-type I-front only occurs for a diffuse GMC (in a spherical homogeneous cloud model); for example, a cloud with $M_{\mathrm{cl}} = 10^5 M_\odot$ and $R_{\mathrm{cl}} = 60$ pc gives $\bar{n}_0 \approx 4.5$ cm^{-3} and $f_{\mathrm{esc}}^{\mathrm{LyC}} \approx 0.72$ in the case of the R-type I-front.

In a realistic dynamical H II region where there is a large temperature contrast between the photoheated H II region and the ambient cold neutral gas, this produces a shock front ahead of the I-front that pushes the gas outward, enabling the I-front (known as D-type) to proceed beyond the Strömgren radius (e.g., Whalen et al. 2004; Krumholz et al. 2007). This allows a dynamical transition from the initially ionization-bound nebula to the density-bound regime at a later time. The D-type I-front expands as $r_I(t) \approx R_S[1 + 7c_{\mathrm{II}} t/(4R_S)]^{4/7}$ (see Shu 1992, Chapter 20) with the velocity of the order of the sound speed of ionized gas $c_{\mathrm{II}} = \sqrt{2k_B T/m_H} = 12.8 T_4^{1/2}$ km s^{-1} and breaks out of the cloud after

$$t_{\mathrm{break}} = \frac{4R_S}{7c_{\mathrm{II}}}\left[\left(\frac{R_{\mathrm{cl}}}{R_S}\right)^{7/4} - 1\right] \text{ for D-type I-front.} \qquad (7)$$

After the breakout of the D-type I-front, because the gas is evacuated by the thermal pressure, the interior density is lowered to $\bar{n}_{\mathrm{II}} = (R_S/r_1)^{3/2}\bar{n}_0$ (Shu 1992). Thus, the resulting density-bound LyC leakage is increased, as there is lower-density gas in the H II region,

$$f_{\mathrm{esc}}^{\mathrm{LyC}} = 1 - \frac{\alpha_B \bar{n}_0}{m_H \epsilon_\star \xi_{\mathrm{ion}}}\left(\frac{\bar{n}_{\mathrm{II}}}{\bar{n}_0}\right)^2 \text{ after D-type breakout.} \quad (8)$$

This gives a high LyC escape fraction for an initially ionization-bound nebula by the action of photoionization heating and the associated I-front shocks.

In Figure 1, we overlay the estimated I-front breakout time for each parameter space of molecular clouds. For most of the observed molecular clouds, H II regions follow the D-type I-front. More luminous and massive GMCs that contribute to the large fraction of the total ionizing photon budget of a galaxy require longer times for the D-type I-front to break out, which must compete with the short, $\sim$Myr lifetime of massive stars. This means that the LyC leakage from the dynamical H II region in a molecular cloud must be treated with fully coupled RHD. Typical ionization parameters at the Strömgren radius and the total hydrogen column density between the Strömgren and cloud radii are approximately $U_S = \dot{N}_{\mathrm{ion}}/(4\pi R_S^2 \bar{n}_0 c) \sim 0.01$ and $\bar{N}_H \sim 10^{22}\,\mathrm{cm}^{-2}$. The turbulent velocities of the massive GMCs of $M_{\mathrm{cl}} \sim 10^{5-6}\,M_\odot$ are $\sigma_v \sim 1-10\,\mathrm{km\,s}^{-1}$.[4] The turbulent nature of the GMCs clearly introduces anisotropy and inhomogeneity to this simple back-of-the-envelope view. Thus, having identified the relevant regime of LyC leakage and the approximate parameter space of interest, we present a detailed account of LyC leakage through a patch of a turbulent molecular cloud in Section 3.

3. Physical Formulation and Simulations

3.1. Equations of RHD

We now turn from a heuristic argument to a physical formulation of LyC leakage and the associated Lyα radiative transfer (RT) in a full RHD framework. We consider a plane-parallel atmosphere (slab) of a turbulent gas cloud around a star-forming region with an initial number density $\bar{n}_0$ and total hydrogen column density $\bar{N}_{\mathrm{H},0}$ (and size $L = \bar{N}_{\mathrm{H},0}/\bar{n}_0$) that is continuously irradiated by the ionizing radiation from a star-forming cluster (see Figure 2). For simplicity, we have assumed a hydrogen-only gas. The system is constantly perturbed on a large scale to maintain the turbulence to represent a large-scale forcing such as gas accretion or disk instability in a galaxy (Elmegreen & Burkert 2010; Goldbaum et al. 2011; Krumholz & Burkhart 2016). This setup was previously employed by Gritschneder et al. (2009, 2010).

The equations of RHD that govern the distribution and kinematics of the gas and the transport of ionizing radiation are

$$\frac{\partial \rho}{\partial t} + \nabla \cdot (\rho \boldsymbol{v}) = 0, \quad (9)$$

$$\frac{\partial \rho \boldsymbol{v}}{\partial t} + \nabla \cdot (\rho \boldsymbol{v} \otimes \boldsymbol{v}) = -\nabla P + \rho \boldsymbol{f}_{\mathrm{stir}} + \rho \boldsymbol{f}_{\mathrm{rad}}, \quad (10)$$
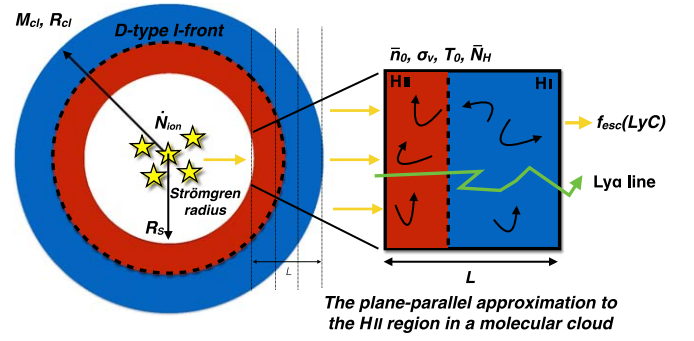

Figure 2. Schematic illustration of the simulation setup. Our simulation boxes represent a patch of the H II region in a GMC irradiated by a single stellar population with an ionizing luminosity $\dot{N}_{\mathrm{ion}}$. Initially, the R-type I-front propagates rapidly to the Strömgren radius R_S, and then the H II region gradually grows by the D-type I-front. A patch of size L located at a distance d from the stellar source is characterized by the initial mean density $\bar{n}_0$, temperature T_0, rms turbulent velocity σ_v, and total gas column density $\bar{N}_H$.

$$\frac{\partial E}{\partial t} + \nabla \cdot [(E + P)\boldsymbol{v}] = \rho \boldsymbol{v} \cdot \boldsymbol{f}_{\mathrm{stir}} + \rho \boldsymbol{v} \cdot \boldsymbol{f}_{\mathrm{rad}} + \Lambda, \quad (11)$$

$$\frac{1}{c}\frac{\partial E_\nu}{\partial t} + \nabla \cdot \boldsymbol{F}_\nu = -n_{\mathrm{HI}}\sigma_{\mathrm{HI}}E_\nu + F_\nu^{\mathrm{inc}}\delta_D(\boldsymbol{r} - \boldsymbol{r}_0), \quad (12)$$

$$\frac{1}{c}\frac{\partial \boldsymbol{F}_\nu}{\partial t} + c\nabla \cdot (\boldsymbol{f}_\nu E_\nu) = -n_{\mathrm{HI}}\sigma_{\mathrm{HI}}\boldsymbol{F}_\nu, \quad (13)$$

which couple to the rate equation,

$$\frac{dn_{\mathrm{HI}}}{dt} = \alpha_B n_p n_e - (\Gamma + \beta_{\mathrm{HI}} n_e)n_{\mathrm{HI}}, \ \Gamma = \int_{\nu_L}^\infty \sigma_{\mathrm{HI}}\frac{F_\nu}{h\nu}d\nu, \quad (14)$$

where ρ, $\boldsymbol{v}$, P, and E are the density, velocity, thermal pressure, and total (internal plus kinetic) energy density of the gas; E_ν and $\boldsymbol{F}_\nu$ ($F_\nu = |\boldsymbol{F}_\nu|$) are the specific energy density and flux of the ionizing radiation; $\boldsymbol{f}_\nu$ is the Eddington tensor; n_{hI} is the number density of neutral hydrogen; $\sigma_{H\mathrm{I}} = \sigma_L(\nu/\nu_L)^{-3}$ is the photoionization cross section of atomic hydrogen ($\sigma_L = 6.3 \times 10^{-18}\,\mathrm{cm}^2$ and $h\nu_L = 13.6\,\mathrm{eV}$); $\beta_{\mathrm{HI}}(T)$ is the collisional ionization rate coefficient; and the force exerted by the ionizing radiation pressure is

$$\boldsymbol{f}_{\mathrm{rad}} = \frac{n_{\mathrm{HI}}}{\rho c}\int_{\nu_L}^\infty \sigma_{\mathrm{HI}}\boldsymbol{F}_\nu d\nu. \quad (15)$$

The heating and cooling are treated approximately. Here $\Lambda = \mathcal{H} + \mathcal{L}$ is the sum of the rates of radiative heating $\mathcal{H}$ and cooling $\mathcal{L}$ in units of energy per unit time per unit volume. The heating term includes H I photoionization heating, and the cooling term includes recombination, collisional ionization and excitation, and bremsstrahlung cooling (Rosdahl et al. 2013). We do not explicitly follow any metal line cooling or other heating/cooling mechanisms. Instead, following Gritschneder et al. (2009), we assume an isothermal equation of state (adiabatic index of $\gamma = 1$) to approximate a complex thermal exchange mechanism such that adiabatic compression and expansion retain the isothermality of the gas.[5]

The external random force field $\boldsymbol{f}_{\mathrm{stir}}$ is applied to excite turbulent flow (e.g., Kritsuk et al. 2007; Federrath et al. 2010).

---

[4] In this case, the gas is subsonic within the H II regions but supersonic for neutral gas ahead of the I-front. When $\sigma_v \gtrsim 12.8T_4^{1/2}\,\mathrm{km\,s}^{-1}$, the gas becomes supersonic in all regions.

[5] In this way, the neutral gas ahead of the I-front remains at the isothermal initial temperature $T_0\,(=100\,\mathrm{K})$, and the photoionized gas retains an approximate isothermality at $\sim 10^4\,\mathrm{K}$.

Table 1
Simulation Setup[a]

Name	$\bar{n}_0$ (cm^{-3})	σ_v (km s^{-1})	$F_{\rm ion}^{\rm inc}$ (photons s^{-1} cm^{-2})	$\bar{N}_{\rm H,0}$ (cm^{-2})	$\mathcal{U}$	$\mathcal{M}_{\rm I,0}$	ζ	Comment
V18S_f2e11_RHD	500	18	2×10^{11}	7.7×10^{21}	0.013	20	1	Fiducial RHD run[b]
V9S_f2e11_RHD	500	9	2×10^{11}	7.7×10^{21}	0.013	10	1	Turbulence series
V2S_f2e11_RHD	500	2	2×10^{11}	7.7×10^{21}	0.013	2	1	Turbulence series
V18S_f2e10_RHD	500	18	2×10^{10}	7.7×10^{21}	0.0013	20	1	Ionizing photon production efficiency series
V18S_f8e10_RHD	500	18	8×10^{10}	7.7×10^{21}	0.0052	20	1	Ionizing photon production efficiency series[c]
V18S_f1e11_RHD	500	18	1×10^{11}	7.7×10^{21}	0.0065	20	1	Ionizing photon production efficiency series
V18S_f4e11_RHD	500	18	4×10^{11}	7.7×10^{21}	0.026	20	1	Ionizing photon production efficiency series
V18S_f8e11_RHD	500	18	8×10^{11}	7.7×10^{21}	0.052	20	1	Ionizing photon production efficiency series
V18C_f2e11_RHD	500	18	2×10^{11}	7.7×10^{21}	0.013	20	0	Compressive forcing
V18S_f2e11_RT	500	18	2×10^{11}	7.7×10^{21}	0.013	20	1	Postprocessed RT[1]
V18S_f2e11_RHD–RP	500	18	2×10^{11}	7.7×10^{21}	0.013	20	1	RHD without radiation pressure[e]

Notes.
[a] For all runs, the size of the simulation box is $L = 5$ pc, and the initial gas temperature is 100 K.
[b] For the fiducial run, $t_{\rm break} \approx 1.1$ Myr, which is converged with respect to the RSLA. However, to ensure the robustness of the conclusion, we express our results in units of $t_{\rm break}$, thereby factoring out the potential sensitivity to the RSLA.
[c] For comparison, we also run a low velocity dispersion simulation with $\sigma_v = 2$ km s^{-1}, keeping all other parameters the same.
[1] The postprocessed RT solves only the RT equations, keeping the density and velocity fields fixed at the initial condition. This effectively corresponds to setting $\nabla P = 0$, $f_{\rm stir} = 0$, and $f_{\rm rad} = 0$ in Equations (10) and (11).
[e] The radiation pressure is switched off by setting $f_{\rm rad} = 0$ in Equations (10) and (11).

We assume a Gaussian random field with a flat power spectrum with power only in the first four largest Fourier modes. We apply a Helmholtz decomposition to the field to produce a different mode (solenoidal or compressive) of large-scale forcing depending on its physical origin, which is parameterized by the forcing parameter ζ ($\zeta = 1$ for purely solenoidal and $\zeta = 0$ for purely compressive). The amplitude of the forcing field is chosen to maintain an rms velocity dispersion of the turbulence of interest. The details are described in Appendix A.

The incident spectrum $F_\nu^{\rm inc}$ from a star-forming region is produced by a starburst based on the binary stellar population synthesis code BPASS (Eldridge et al. 2017). The important dimensionless number is the ionization parameter at the incident face,

$$\mathcal{U} = \frac{F_{\rm ion}^{\rm inc}}{\bar{n}_0 c} = \frac{1}{\bar{n}_0 c} \int_{\nu_L}^{\infty} \frac{F_\nu^{\rm inc} d\nu}{h\nu}. \tag{16}$$

For example, at the ionization parameter $\mathcal{U} = 1.3 \times 10^{-2}$ and $\bar{n}_0 = 500$ cm^{-3}, the incident flux is $F_{\rm ion}^{\rm inc} = 2 \times 10^{11}$ s^{-1} cm^{-2}. This corresponds to a slab located $\simeq 2$–10 pc away from a single stellar population with an ionizing photon production rate of $\simeq 10^{50}$–10^{51} s^{-1}. These values roughly match with those found in global simulations of $\sim 10^4$–$10^6 M_\odot$ GMCs (e.g., Geen et al. 2015, 2016; Kim et al. 2018).

Using the line-of-sight H I column densities $N_{\rm HI}$ measured from the outcoming face of the slab, the LyC leakage is defined as the transmitted fraction of ionizing photons with frequency ν,

$$\mathcal{T}_{\rm LyC}(\nu) = \int_0^\infty e^{-\sigma_{\rm HI} N_{\rm HI}} P(N_{\rm HI}) dN_{\rm HI}, \tag{17}$$

where $P(N_{\rm HI})$ is the probability distribution function (PDF) of $N_{\rm HI}$ column densities along all sight lines. By integrating over all photons escaping from the slab, the LyC escape fraction is given by

$$f_{\rm esc}^{\rm LyC} = \frac{\int_{\nu_{\rm HI}}^\infty \mathcal{T}_{\rm LyC}(\nu) \frac{F_\nu^{\rm inc}}{h\nu} d\nu}{\int_{\nu_{\rm HI}}^\infty \frac{F_\nu^{\rm inc}}{h\nu} d\nu}. \tag{18}$$

Note that the escape fraction can also be measured by directly taking the ratio between incoming and outcoming fluxes. Both $N_{\rm HI}$- and flux-based estimators agree well (Trebitsch et al. 2017). We also verified that our frequency-dependent definition gives consistent results with the frequency-integrated RHD simulations. We use the $N_{\rm HI}$-based estimator, Equations (17) and (18), to measure the LyC escape fraction throughout this paper.

3.2. RHD Turbulence Simulations

We simulate the above problem using RAMSES-RT (Teyssier 2002; Rosdahl et al. 2013). It employs a second-order Godnouv method to solve an Eulerian fully coupled RHD on an adaptive mesh refinement grid, and the RT is solved by the moment method. We use a static uniform grid with 128^3 resolution with a box of $L = 5$ pc on a side. We use the MUSCL scheme with the HLLC solver for hydrodynamics with the MinMod slope limiter and a Courant time-step factor of 0.1. For the isothermal equation of state, we set the adiabatic index close to unity $\gamma \approx 1$ to avoid division by zero. For radiative transport, the HLL solver is used to accurately track the shadowing behind dense gas. We use a single frequency group integrated over 13.6 eV $< h\nu <$ 24.6 eV, the M1 closure for the Eddington tensor, and the on-the-spot approximation. We used the reduced speed-of-light approximation (RLSA) with $10^{-3}c$ to avoid a prohibitively long time integration. We have also tested the convergence with $10^{-2}c$ for a fiducial model and found the converging results.

To perform the RHD turbulence simulations, we have first generated initial conditions by running isothermal turbulence simulations without RT. We set the initial density to $\bar{n}_0 = 500$ cm^{-3} and temperature $T_0 = 100$ K with the periodic
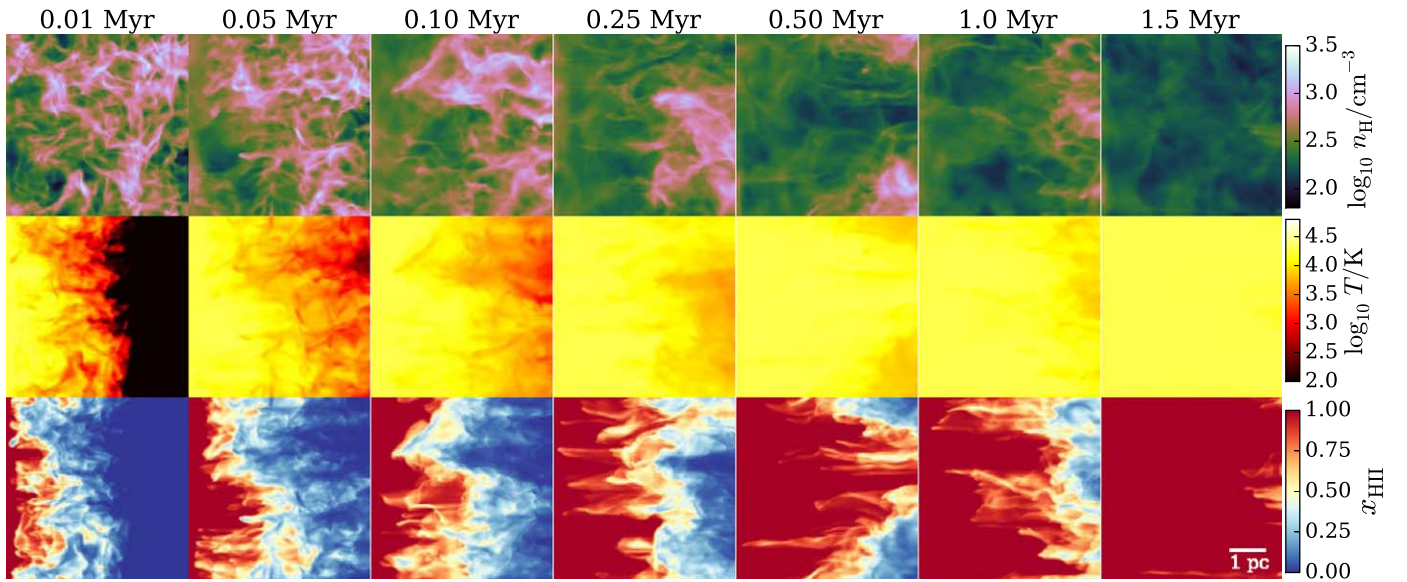
Figure 3. Projected maps (side view) of gas density $n_{\rm H}$, mass-weighted temperature T, and ionized fraction $x_{\rm HII}$ as a function of time from left to right (shown is the run `V18S_f2e11_RHD`). The map is 5 pc side^{-1}, and the 1 pc length is indicated at the bottom right corner. The ionizing radiation is coming from the left boundary in all panels. An animated version of this figure is downloadable from http://www.star.ucl.ac.uk/~kakiichi/.
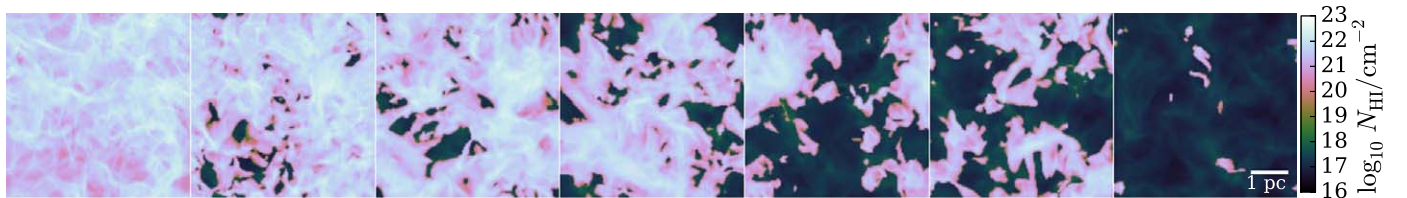

Figure 4. Projected maps (when viewed from the outflow boundary face) of H I column density $N_{\rm HI}$ as a function of time from left to right (as in Figure 3, the snapshots at $t = 0.1, 0.05, 0.10, 0.25, 0.50, 1.0,$ and 1.5 Myr of `V18S_f2e11_RHD` are shown). The viewing direction is toward the nonperiodic outcoming face.

boundary condition at all faces. In order to drive turbulence, we perturb the flow with a Gaussian random field with power only at large scales following the method of Robertson & Goldreich (2012, 2018; see Appendix A) with an appropriate choice of the forcing parameter; we set $\zeta = 1$ for a fiducial run. We evolve the system for a few tens of Eddy turnover times $\sim 10 T_{\rm eddy}$, where $T_{\rm eddy} = L/(2\sigma_v)$, to ensure that the statistical steady state is reached. We then use the snapshot after $2 T_{\rm eddy}$ time as an initial condition for the corresponding RHD turbulence simulation.

Using the initial condition, we then restart the simulation with full RHD. Both turbulence driving and RT are activated. The box is irradiated from the left boundary with an ionizing flux $F_{\rm ion}^{\rm inc} = 1\text{–}4 \times 10^{11}$ s^{-1} cm^{-2} (the corresponding ionization parameters are shown in Table 1). We use the spectrum-integrated cross section corresponding to the spectral shape of the incoming ionizing radiation consistent with the BPASS stellar population synthesis code. We set a reflective boundary condition at the left boundary face and an outflow boundary condition at the right boundary face but otherwise set a periodic boundary condition. We then evolve the system for 2 Myr. In order to investigate the conditions for LyC leakage, we have varied the simulation setup and parameters, which are summarized in Table 1.

3.3. Monte Carlo Lyα RT

We employ the Monte Carlo RT code TLAC (Gronke & Dijkstra 2014). Monte Carlo RT codes track individual photon

packages on their trajectory while simultaneously keeping track of their frequency. This includes the change of direction and the shift in frequency (mostly) due to Doppler shifting during a scattering event and a bulk motion (see, e.g., Dijkstra 2017).

As input, we used the simulated H I number density, temperature, and velocities on the Cartesian grid with a spatial resolution equal to the RAMSES-RT runs. We injected Lyα photons at the line center from the left boundary of the box ($x = 0$). We employed $\sim 10^4$ photon packets with a dynamical core-skipping scheme (Smith et al. 2015). The emergent Lyα line profile is composed of the frequencies of the photons escaping in the positive x-direction. To include the backscattering, we have mirrored the structure around the $x = 0$ axis. Thus, in practice, the Lyα RT is done on the $256 \times 128 \times 128$ grid with a source at the $x = 0$ plane. For the y and z boundaries, we used a periodic boundary condition. Therefore, our simulated geometry corresponds to that of a semi-infinite slab (Neufeld 1990).[6]

We ignore the contribution from the Lyα emission by the recombination within the simulated volume. As we expect that the Lyα photons are generated at a denser inner region in a

---

[6] We expect that the difference between semi-infinite slab and spherical geometry gives rise to the difference in peak separation by $\sim 20\%$ based on the analytic solutions (Adams 1972; Neufeld 1990; Dijkstra et al. 2006). On the other hand, slab geometry has the advantage of being able to more accurately capture the shadowing effect of ionizing radiation in the moment-based RT method because the shadowing structure aligns with the grids, whereas a spherical geometry more easily suffers from numerical diffusivity because of the nonalignment between shadows and grids. As the mechanism for creating ionized channels is critical for the escape of ionizing and Lyα photons, for the purpose of numerical experiments, we adopted the slab geometry.

realistic H II region, we believe that neglecting the emission within a simulated volume is a fair first approximation. The Lyα emission within a volume would likely increase the contribution from a density-bounded channel (ionized) to the total Lyα line profile. We defer a detailed study to future work. For the purposes of our idealized numerical experiments, we adopt this simple approach.

4. Results

4.1. LyC Escape Fraction

Here we present an overview of the LyC leakage from a (patch of) the H II region in turbulent molecular clouds. In Figure 3, we show the time evolution of the RHD turbulence.

Ionizing radiation propagates anisotropically. The photons race ahead in the directions of low column densities opened up by the turbulent fluctuations. The D-type I-fronts do so by creating shocks by the photoheating across the H II region and the ambient neutral medium, which evacuates the gas effectively in the low column density channels. Figure 4 confirms the presence of channels of leaking radiation. As supersonic turbulence changes its structure faster than the speed of the D-type I-front of the order of the sound speed of the ionized gas, the low column density channels are not opened long enough to sustain the escape of ionizing radiation in the same directions. Instead, the system changes the structure of escaping channels over the Eddy turnover timescale $T_{\text{eddy}} \approx 245(L/5 \text{ pc})(\sigma_v/10 \text{ km s}^{-1})^{-1}$ kyr. The I-fronts drastically slow down or even halt as soon as dense clumps and filaments are created ahead of them by supersonic shocks in turbulence. That is, LyC photons in a driven turbulent medium need to propagate through a dynamic, constantly changing "maze" before leaking out of the system.

These turbulent fluctuations introduce the stochastic variability in the escape fraction on the $\sim$100 kyr timescale. The time evolution of the escape fraction is shown in Figure 5. For example, the peak at $\simeq$0.5 Myr corresponds to the timing of the opening of a large channel (see Figure 3). Note that this turbulent variability is smaller than the longer $\sim$10 Myr timescale variability associated with the supernova feedback that exhibits a large $f_{\text{esc}}^{\text{LyC}}$ variation, as the inactive phase of the feedback can completely shut off the leakage.

While the turbulent fluctuations allow LyC photons to leak out at an early time, the timing at which the breakout of the average I-fronts occurs is delayed. In simulations, we define the breakout time as a time when more than 95% of the entire medium is ionized. This gives $t_{\text{break}} \approx 1.1$ Myr for the fiducial RHD run. For a homogeneous slab, the breakout time of the D-type I-front can be computed analytically,

$$t_{\text{break}} = \frac{4}{5}\frac{c}{c_{\text{II}}}t_{\text{rec}}\mathcal{U}\left[\left(\frac{\alpha_{\text{B}}N_{\text{H}}}{c\,\mathcal{U}}\right)^{5/4} - 1\right] \sim 0.6 \text{ Myr}, \quad (19)$$

for the same parameters used in the fiducial run. Evidently, the average I-front breakout time is delayed for a turbulent medium. There are two reasons for this delay in the breakout time. When the rms turbulent velocity in the H II region remains supersonic ($\sigma_v > c_{\text{II}} \approx 12.8T_4^{1/2}$ km s^{-1}), the density fluctuations can enhance the recombination rate, causing the slowdown of the average I-fronts. In addition, the I-front shock–turbulence interaction transports the warm neutral gas
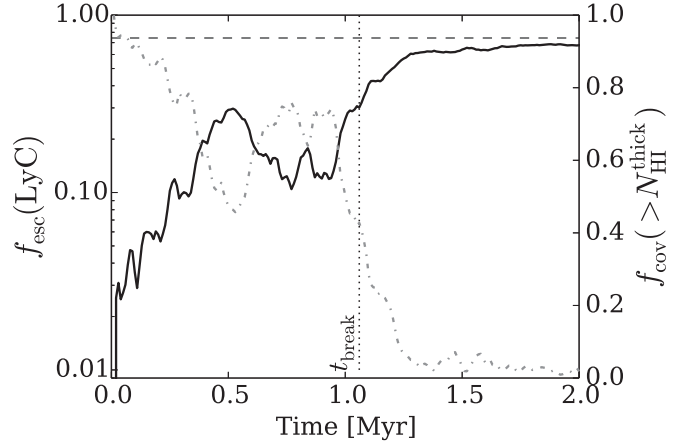

Figure 5. Time evolution of the LyC escape fraction (solid line, left y-axis) and covering fraction of optically thick gas $N_{\text{HI}} > 7.3 \times 10^{17}$ cm^{-2} (dashed–dotted line, right y-axis) in the V18S_f2e11_RHD run. The vertical dotted line indicates the I-front breakout time $t_{\text{break}} \approx 1.1$ Myr. The asymptotic analytic limit of the LyC escape fraction for a fully density-bound nebula, Equation (21), is indicated by the horizontal dashed line.

ahead of the I-front. This increases the thermal pressure of the ambient gas into which the D-type I-front is propagating. This decrease in the thermal pressure gradient and the additional turbulent ram pressure may also contribute to the slowdown of the average speed of the D-type I-front (Tremblin et al. 2014; Geen et al. 2015).

After the breakout $t > t_{\text{break}}$, LyC leakage is regulated by the balance between the recombination rate in the H II region and the incident ionizing flux from the source, approaching the asymptotic value set by the density-bound regime. The time variability settles down as the medium becomes fully ionized and the gas evacuates the box. Since the mechanism of escape is different before and after the breakout that is dominated by either the ionization-bound or density-bound LyC leakage, it is convenient to understand the leaking mechanism in units of the breakout time. We follow this convention in the rest of the paper.

4.2. Covering Fraction, Kinematics, and Ionizing Photon Production Efficiency

The leakage through the turbulent H II regions introduces the correlation of LyC escape fraction with the H I covering fraction, kinematics, and ionizing photon production efficiency.

The PDFs of the H I column densities in Figure 6 show the two clear channels of LyC photons: one corresponding to the photoionized density-bound channels ($N_{\text{HI}} \approx 10^{17-18}$ cm^{-2}) where LyC escapes and another corresponding to the neutral ionization-bound channels ($N_{\text{HI}} \approx 10^{21-22}$ cm^{-2}) where the I-fronts still reside within the system. As LyC photons escape through narrow photoionized channels, a large fraction of hydrogen can be retained in a neutral phase, allowing high LyC leakage with a high average H I column density $\langle N_{\text{HI}} \rangle$ (see Figure 7). As a result, the $\langle N_{\text{HI}} \rangle$ of a system may not give a clear indicator of LyC leakage.

The quantity that is better correlated with the LyC escape fractions is the H I covering fraction. We define the covering fraction, $f_{\text{cov}}(> N_{\text{HI}})$, as the fraction of sight lines with H I column densities greater than N_{HI}. We compute the covering fraction of optically thick sight lines with less than 1% leakage
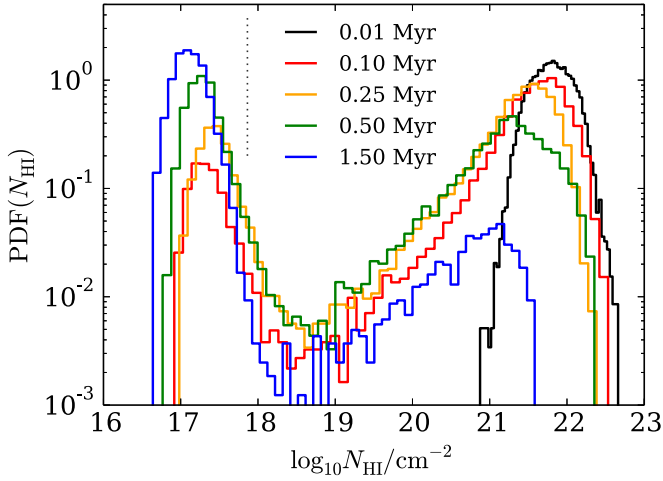
Figure 6. The PDF of the H I column densities, N_{HI}, at 0.01, 0.10, 0.25, 0.50, and 1.50 Myr in the V18S_f2e11_RHD run. The column density at which a channel becomes optically thick with less than 1% LyC leakage at the Lyman limit is indicated by the vertical dotted line.
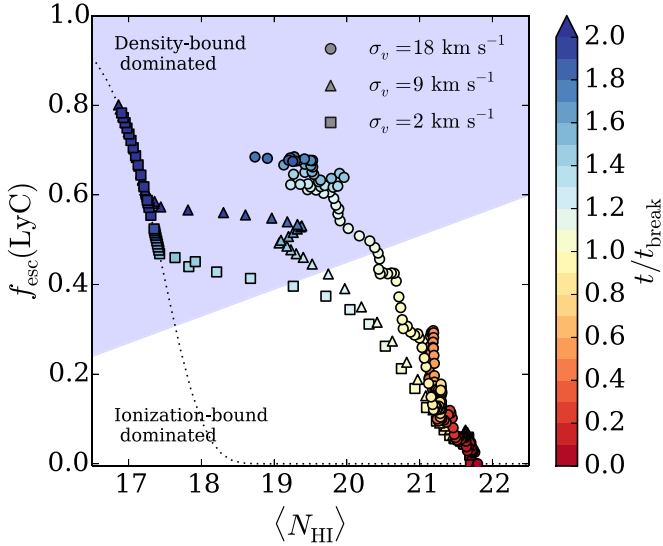

Figure 7. Correlation between LyC escape fraction and average H I column density $\langle N_{HI} \rangle$ of the H II regions. The results from three runs (squares: V2S_f2e11_RHD; triangles: V9S_f2e11_RHD; circles: V18S_f2e11_RHD) are shown. The colors indicate the time normalized by the I-front breakout time of each simulation, t/t_{break}. The dotted line indicates the escape fractions for homogeneous media at each $\langle N_{HI} \rangle$, $f_{esc}^{LyC} = \frac{\int_{\nu_{HI}}^{\nu_{HeI}} e^{-\sigma_{HI}\langle N_{HI}\rangle} F_\nu^{inc}/(h\nu)d\nu}{\int_{\nu_{HI}}^{\nu_{HeI}} F_\nu^{inc}/(h\nu)d\nu}$. The shaded region marks the approximate transition between nebulae dominated by density- and ionization-bound channels. The figure shows that the turbulent H II regions allow high LyC escape fractions as the photons leak through narrow holes but retain high average H I column densities over the entire system.

at the Lyman limit[7] corresponding to an H I column density more than $N_{HI}^{thick} = -\sigma_L^{-1} \ln 0.01 \simeq 7.3 \times 10^{17}$ cm^{-2}.

Figure 8 shows the correlation between the LyC escape fraction and the covering fraction. Before the breakout of the average I-front, LyC escape is directly correlated with the H I covering fraction, which leads to a linear relation $f_{esc}^{LyC} \propto 1 - f_{cov}(>N_{HI}^{thick})$. However, as the photoionized channels are

not empty, the escape fraction is lower because photons recombine inside them, causing $f_{esc}^{LyC} < 1 - f_{cov}(>N_{HI}^{thick})$. While a low covering fraction is a necessary condition for high LyC leakage, a measure of the covering fraction places only an upper limit on the escape fraction (Vasei et al. 2016).

The turbulent kinematics also influences the properties of the photoionized channels. For increasing turbulent velocities, there is a larger probability for lower densities to occur, which leads to less recombination within the channels. This further implies a higher LyC escape fraction at a given covering fraction. The resulting relation is therefore the combination of covering and transmitted fractions of LyC photons through the photoionized channels,

$$f_{esc}^{LyC} \approx f_{tr}(\sigma_v)[1 - f_{cov}(>N_{HI}^{thick})]. \quad (20)$$

In our simulations, we find that the transmitted fractions are $f_{tr}(\sigma_v) \approx \{0.28, \; 0.36, \; 0.55\}$ for $\sigma_v = \{2, \; 9, \; 18\}$ km s^{-1} by fitting the linear relation to the numerical results.

After the average breakout of the I-fronts, because the system is dominated by density-bound channels, there is little correlation between the escape fraction and the covering fraction. The escape fraction is now regulated by the recombination rate in the H II region. At the density-bound dominated regime, the escape fraction is set by the balance between incident ionizing flux and recombination rate in the photoionized medium,

$$f_{esc}^{LyC} \approx 1 - \frac{\alpha_B L}{F_{ion}^{inc}} \int n_e^2 P_V(n_e|\mathcal{M}_{II})dn_e, \quad (21)$$

where $P_V(n_e|\mathcal{M}_{II})$ is the volume-weighted density PDF of the ionized gas with a Mach number $\mathcal{M}_{II}$.

In Figure 9, we show the relation between the escape fraction and the incident ionizing flux. At the density-bound dominated regime, the escape fraction increases with the incident ionizing flux (ionizing photon production efficiency), as expected from Equation (21) (see Section 2). The ionizing photon production efficiency of the stellar population affects the LyC escape as harder sources induce more photoionization, making it easier for photons to escape. This intrinsic dependence of the LyC escape fraction on ionizing photon production efficiency means that spectrally harder sources, common for higher redshifts and fainter objects (e.g., Matthee et al. 2017; Harikane et al. 2018), may be able to deposit more ionizing photons into the surroundings because both the LyC escape fraction and ionizing photon production efficiency can increase the total escaping LyC luminosity, $\propto f_{esc}^{LyC}\langle\xi_{ion}\rangle\xi_{ion}$ SFR.

While the escape fraction can consistently be $>10\%$ after the breakout, a higher level of turbulence will somewhat reduce the LyC escape in the density-bound dominated regime (see Figure 9). When the turbulent fluctuations are supersonic inside the H II region, the density fluctuations introduce the clumping of gas with an associated clumping factor,[8]

$$\mathcal{C}(\mathcal{M}_{II}) = \frac{\langle n_e^2 \rangle}{\bar{n}_e^2} = \int_{-\infty}^{\infty} \left(\frac{n_e}{\bar{n}_e}\right)^2 P_V(n_e|\mathcal{M}_{II})dn_e,$$
$$\approx 1 + (\mathcal{M}_{II}/3)^2. \quad (22)$$

---

[7] The Lyman limit column density $N_{HI}^{LL} = 1/\sigma_L^{-1}$ is the value at which the gas starts to be optically thick, but at the column density, the transmission $e^{-1} \approx 0.37$ is still appreciably large.

[8] The approximate equality is derived using the lognormal density PDF for solenoidal turbulence (e.g., Federrath et al. 2010). In our simulations, assuming the lognormal PDF for the ionized gas gives a clumping factor accurate to $\sim 5\%$ to the simulated value.
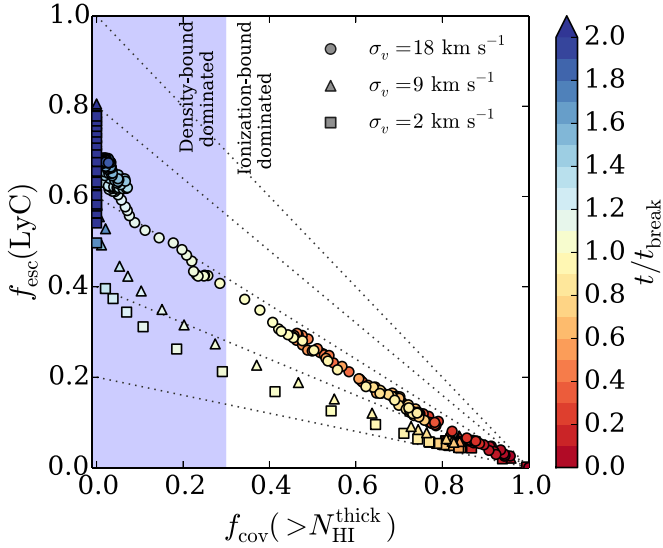
Figure 8. Correlation between LyC escape fraction and covering fraction of optically thick gas. The results from three runs (squares: V2S_f2e11_RHD; triangles: V9S_f2e11_RHD; circles: V18S_f2e11_RHD) are shown. The colors indicate the time normalized by the I-front breakout time of each simulation, $t/t_{\rm break}$. Linear relations, $f_{\rm esc}^{\rm LyC} \propto 1 - f_{\rm cov}$, with different slopes, 0.2, 0.4, 0.6, 0.8, and 1.0, are indicated by dotted lines. The shaded region marks the approximate transition between nebulae dominated by ionization- and density-bound channels before and after the breakout of the average I-front.
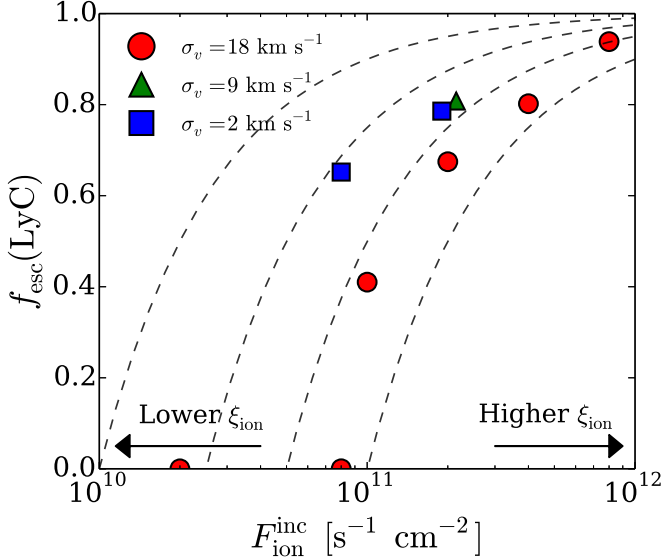

Figure 9. Correlation between LyC escape fraction and incident ionizing flux $F_{\rm ion}^{\rm inc}$ (a proxy for ionizing photon production efficiency $\xi_{\rm ion}$) at the end of the simulations (2 Myr). For all points except the first two red points, the average I-fronts have already broken out for all simulations, therefore indicating the LyC escape fractions at the density-bound dominated limit. The first two red points are zero, as the I-front does not break out before the end of the simulation. The dashed lines indicate the expected scaling of $f_{\rm esc}^{\rm LyC}$ with $F_{\rm ion}^{\rm inc}$ in the density-bound leakage, $f_{\rm esc}^{\rm LyC} = 1 - ({\rm const.})/F_{\rm ion}^{\rm inc}$.

This leads to a reduction of the escape fraction due to the enhanced recombination rate. For the $\sigma_v = 18\,{\rm km\,s^{-1}}$ RHD turbulence simulation, we find $\mathcal{M}_{\rm II} \approx 1.1$ and the clumping factor $\mathcal{C}(\mathcal{M}_{\rm II}) \approx 1.2$ in the photoionized gas. The effect only becomes prominent for a very high value of turbulent velocity dispersion $\sigma_v > 12.8T_4^{1/2}\,{\rm km\,s^{-1}}$ that can maintain supersonic

fluctuations in the photoheated gas $\mathcal{M}_{\rm II} > 1$. For a modest velocity dispersion $\sigma_v < 12.8T_4^{1/2}\,{\rm km\,s^{-1}}$, e.g., in the Milky Way–like GMCs, the photoionized gas remains subsonic, $\mathcal{M}_{\rm II} < 1$. Because the thermal gas pressure smooths out the density perturbations within a few sound-crossing timescales faster than turbulent mixing, the density clumping is modest (Konstandin et al. 2012). Indeed, in the simulations with $\sigma_v = 2,\ 9\,{\rm km\,s^{-1}}$ ($\mathcal{M}_{\rm II} = 0.1,\ 0.6$), the clumping factors of the ionized gas remain as $\mathcal{C}(\mathcal{M}_{\rm II}) = 1$. Subsonic turbulence inside the H II region thus has a negligible effect on the density-bound value of the LyC escape fraction.

In both the density- and ionization-bound dominated regimes, turbulent H II regions introduce a diversity in $f_{\rm esc}^{\rm LyC}$ for a given H I covering fraction and ionizing photon production efficiency.

4.3. Role of Turbulence and Radiative Feedback

The presence of turbulence alone is not a sufficient condition to trigger high LyC leakage. The radiation–hydrodynamical coupling, the ability to ionize the gas beyond the classical Strömgren radius by the D-type I-front, and radiative feedback are important for regulating LyC leakage through a turbulent GMC.

To illustrate this point, we compare a simulation in which the radiation–hydrodynamical coupling is switched off (i.e., postprocessed RT) with the fiducial run with the same initial turbulence. As there is no dynamical response of gas by photoionization or radiation pressure, the I-front remains as the R-type in the postprocessed RT. In this case, if the initial gas column density is larger than

$$N_{\rm H,0} > \frac{F_{\rm ion}^{\rm inc}}{\alpha_B \bar{n}_0} \approx 1.15 \times 10^{21} T_4^{0.7} \left(\frac{\mathcal{U}}{10^{-2}}\right) {\rm cm}^{-2}, \quad (23)$$

the I-front is kept trapped within a cloud. This is the regime similar to that studied by Safarzadeh & Scannapieco (2016). Comparison with the fiducial run is shown in Figure 10. After several recombination times, the R-type I-front reaches a steady state and is effectively frozen in. Although the turbulence density fluctuations create lower column density channels by a few orders of magnitude around the mean (e.g., Federrath et al. 2010), there remains a substantial optical depth even along the lowest column density channels. Thus, the total increase in LyC escape by turbulent fluctuations remains modest. For example, we find only $f_{\rm esc}^{\rm LyC} \simeq 0.008$ in the R-type I-front simulation by postprocessing RT, whereas the full RHD simulation of the D-type I-front can reach $f_{\rm esc}^{\rm LyC} \gtrsim 0.10$ after ~ 1 Myr. The photoheating across the I-front and the associated shocks offer an effective means for LyC photons to evacuate efficiently through low column density channels.

The inefficiency of turbulent fluctuations when creating $N_{\rm HI} < 10^{17}\,{\rm cm}^{-2}$ channels is not surprising, as the typical surface densities of GMCs are $\Sigma_{\rm cloud} \sim 10–1000\,M_\odot\,{\rm pc}^{-2}$ (see Leroy et al. 2015, for a recent compilation and references therein), corresponding to the total hydrogen column density from the center of the spherical cloud to the outer radius, $N_{\rm H} = (3/4)(\Sigma_{\rm cloud}/m_{\rm H}) \sim 10^{21}–10^{23}\,{\rm cm}^{-2}$. This means that about $4–7$ orders of magnitude fluctuations in column densities within a cloud are required to produce $N_{\rm HI} \lesssim 10^{17}\,{\rm cm}^{-2}$
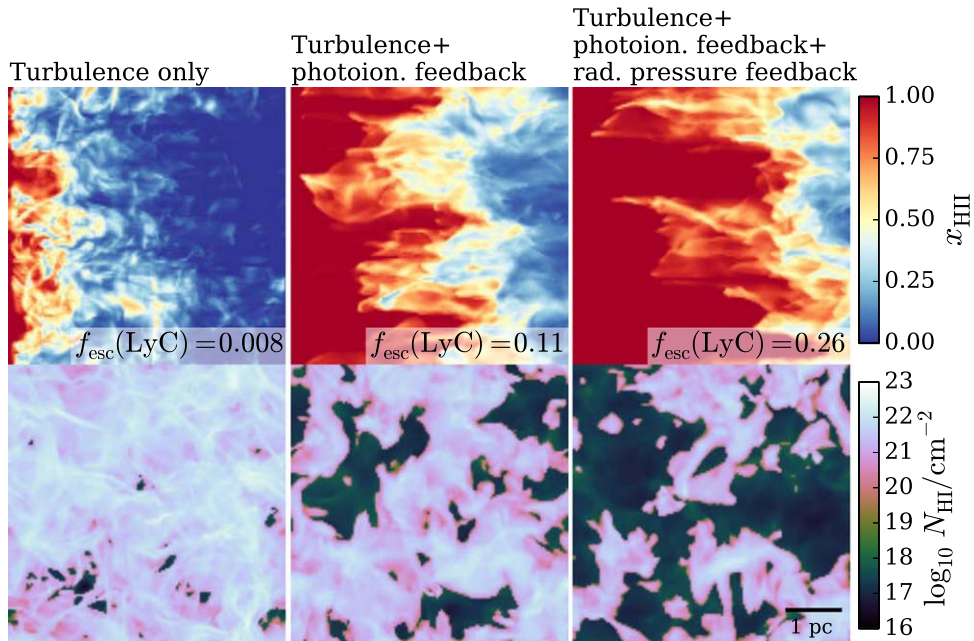
Figure 10. Effect of turbulence and radiative feedback on LyC leakage. Shown are the projected maps of the mass-weighted ionized fractions and H I column densities in the three simulations (left: `V18S_f2e11_RT`, postprocessed RT (turbulence only); middle: `V18S_f2e11_RHD-RP`, RHD without radiation pressure (turbulence + photoionization feedback); right: `V18S_f2e11_RHD`, full RHD (turbulence + photoionization feedback + radiation pressure feedback)) at 1 Myr. The LyC escape fractions are indicated at the bottom right corner of each top panel.

channels. In fact, following Brunt et al. (2010a, 2010b) and Thompson & Krumholz (2016), we can estimate the fraction of I-fronts being trapped in turbulence without radiative feedback as

$$f_{\rm trap} = \int_{s_{\rm trap}}^{\infty} P_{\rm H\,I}(s|\mathcal{M}_{\rm I})ds = \frac{1}{2}\,{\rm erfc}\left[\frac{\sigma_{\ln N_{\rm H}}^2 + 2s_{\rm trap}}{\sqrt{8\sigma_{\ln N_{\rm H}}^2}}\right], \quad (24)$$

where $P_{\rm H\,I}(s|\mathcal{M}_{\rm I})$ is the lognormal probability distribution of column density and $s_{\rm trap} = \ln(N_{\rm H}^{\rm trap}/\bar{N}_{\rm H})$ with $N_{\rm H}^{\rm trap} \approx 1.15 \times 10^{21}\,{\rm cm}^{-2}$ (see Equation (23)). The standard deviation is given by

$$\sigma_{\ln N_{\rm H}}^2 \approx \ln[1 + R(\mathcal{M}_{\rm I}/3)^2)], \quad (25)$$

and $R = \frac{1}{2}\left(\frac{3-\alpha}{2-\alpha}\right)\left(\frac{1-\mathcal{M}_{\rm I}^{2(2-\alpha)}}{1-\mathcal{M}_{\rm I}^{2(3-\alpha)}}\right)$ with $\alpha = 2.5$ being the power-law index of the density power spectrum $P(k) \propto k^{-\alpha}$ (e.g., Krumholz 2014, for a review). The estimate suggests that only $1 - f_{\rm trap} \approx 0.06\%$ of I-fronts in the $\mathcal{M}_{\rm I} \approx 10$ gas in an $\bar{N}_{\rm H} \approx 10^{22}\,{\rm cm}^{-2}$ cloud can exit the system. For $\mathcal{M}_{\rm I} \approx 20$, the fraction is still $1 - f_{\rm trap} \approx 1\%$. Although a higher Mach turbulence and the associated increase in intermittency would open up more low column density channels (Hopkins 2013; Federrath 2013), substantial LyC escape still requires radiative feedback in addition to turbulence (see Figure 10).

Among the two radiative feedback mechanisms—photoionization heating and radiation pressure—the direct ionizing radiation pressure plays a secondary role in evacuating the gas through the low column density channels, in agreement with previous studies (Rosdahl & Teyssier 2015). The relative importance of photoionization and radiation pressure is easy to understand by taking the thermal-to-radiation pressure ratio

(Lopez et al. 2014; McLeod et al. 2019),

$$\frac{P_{\rm th}}{P_{\rm rad}} = \frac{2k_B n_e T}{\langle h\nu \rangle F_{\rm ion}^{\rm inc}/c}$$

$$\approx 3.8 T_4 \left(\frac{n_e}{200\,{\rm cm}^{-3}}\right)\left(\frac{F_{\rm ion}^{\rm inc}}{2 \times 10^{11}\,{\rm s}^{-1}\,{\rm cm}^{-2}}\right)^{-1}. \quad (26)$$

The impact of ionizing radiation pressure is less effective than thermal pressure by photoionization heating even in the plane-parallel geometry, which will be reduced further in a spherical geometry by the geometric factor of r^{-2}. The Lyα radiation pressure may be important, although the exact degree of the impact is still unclear (Dijkstra & Loeb 2008, 2009; Smith et al. 2017; Kimm et al. 2018). In the regimes studied, the shocks induced by photoionization heating and turbulent fluctuations are likely the major modes of regulating the opening of low column density channels. In summary, we find that turbulence is not the sole agent to regulate LyC leakage in the H II regions. Radiative feedback *and* turbulence are what regulate the LyC leakage; in particular, the photoheated I-front shock provides an effective means for evacuating the gas through the openings of turbulence-generated channels.

5. Lyα–LyC Connection

5.1. Physics of Lyα Line Formation

The Lyα line profiles emerging from the RHD turbulence depend on the properties of LyC leakage. The details of Lyα transfer are described elsewhere (see, e.g., Dijkstra 2017). Here we summarize the relevant aspects of Lyα line formation for LyC-leaking turbulent H II regions.

The LyC leakage through RHD turbulence produces the two distinctive passages for Lyα photons: one with low column densities $N_{\rm HI} \approx 10^{17-18}$ cm^{-2} allowing LyC escape (density-bound channels) and another with $N_{\rm HI} \approx 10^{21-22}$ cm^{-2} that remains optically thick to LyC (ionization-bound channels; see Figure 6). This bimodal H I distribution corresponds to that of the "picket-fence" or "holes" model often used to interpret observations (Zackrisson et al. 2013; Reddy et al. 2016; Steidel et al. 2018). Here such geometry of H I gas arises naturally as a consequence of the RHD turbulence.

The Lyα optical depth at a frequency $x = (\nu - \nu_\alpha)/\Delta\nu_D$ is $\tau_\alpha = \tau_{\alpha,0}\phi(x)$, where ν_α is the resonant frequency, $\Delta\nu_D = \nu_\alpha b/c$ is the Doppler width (b is the Doppler b-parameter), $\phi(x)$ is the Voigt profile, $\tau_{\alpha,0} = \sigma_{\alpha,0}N_{\rm HI}$ is the optical depth at line center, and $\sigma_{\alpha 0} \approx 5.9 \times 10^{-14}T_4^{-1/2}$ cm^2 is the line center Lyα cross section. The gas above the H I column density,

$$N_{HI} > 1/\sigma_{\alpha,0} \approx 1.7 \times 10^{13}T_4^{1/2} \text{ cm}^{-2}, \tag{27}$$

is optically thick to the photons emitted at line center. Therefore, Lyα photons are more susceptible to the amount of (residual) neutral hydrogen compared to the column density ($N_{\rm HI} \lesssim 10^{17-18}$ cm^{-2}) required for LyC photons to escape. For example, in the fiducial simulation, the photoionized LyC escaping channels (having the residual H I fractions, $x_{\rm HI} \approx \alpha_B n_{\rm H}/\Gamma \sim 10^{-4}-10^{-5}$, and the gas density, $n_{\rm H} \sim 200$ cm^{-3}) have an average H I column density of

$$\bar{N}_{H{\rm I,channel}} \approx 2.4 \times 10^{17} \text{ cm}^{-2}, \tag{28}$$

filling up $1-f_{\rm cov}$ fraction of sight lines around ionizing sources. The Lyα photons emitted at the line center therefore cannot freely stream out. Instead, they experience appreciable scattering events before escape. The resulting Lyα profile is therefore strongly influenced by the availability, H I column density, and kinematics of LyC escape channels.

The turbulence also introduces both density and velocity fluctuations that would influence the fate of the Lyα photons. Gronke et al. (2016, 2017) detailed the Lyα transfer mechanism through a clumpy medium and found that Lyα photons can escape via either (i) a "single flight" or "excursion" after core or wing scatterings, i.e., similar to a homogeneous slab (Osterbrock 1962; Adams 1972), or (ii) a "random walk" between clumps (Hansen & Oh 2006). These two different modes of Lyα escape subsequently leave an imprint on the emergent Lyα spectrum, most easily identified by the flux at line center. Since the filling factor of the optically thick gas to Lyα photons is high both inside the H II region and in the underdense regions of turbulence, there is little room for Lyα photons to freely travel between the clumps in a turbulent H II region. Therefore, for our parameter space studied, the photons escape primarily by the former mechanism, i.e., via single flight or excursion.[9] If the H I column density of a channel is optically thick to the Doppler core but optically thin to the Lorentzian wing, Lyα photons escape via a single flight after the frequency is shifted out of the core. Such escape is dominant in low-$N_{\rm HI}$ channels with (Osterbrock 1962;

---

[9] Although we find Lyα escape mostly via a single flight or excursion, we expect that the contribution from escape via random walk may increase if extreme turbulence maintains a high level of density fluctuations in the H II region. Then, Lyα escape via random walk through clumpy channels will contribute to the residual nonzero flux at line center.
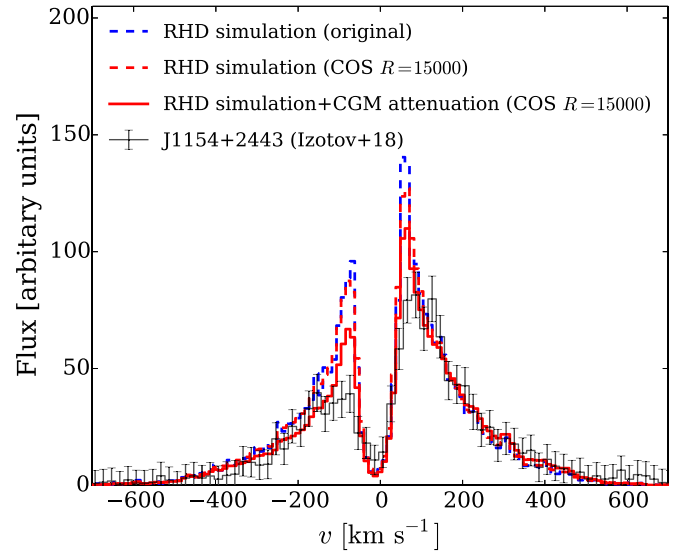

Figure 11. Comparison of the emergent Lyα line profile from the RHD turbulence simulation (V18S_f2e11_RHD at $t = 0.5$ Myr) with the observed COS spectrum of a LyC-leaking galaxy, J1154+2443 (Izotov et al. 2018a). The three simulated spectra correspond to one at the spectral resolution of the simulation (blue dashed line), one at the COS resolution ($R = 15,000$; red dashed line), and one with the CGM attenuation model of Kakiichi & Dijkstra (2018) at the COS resolution (red solid line). Regardless of the additional uncertainty from the CGM, Lyα transfer through the turbulent LyC-leaking H II region can explain the observed spectrum reasonably well.

Zheng & Miralda-Escudé 2002)

$$N_{HI} \lesssim \frac{1}{\sigma_{\alpha,0}\phi(x_*)} \approx 7 \times 10^{17} \text{ cm}^{-2}, \quad \begin{array}{l}\text{escape via single flight} \\ \text{after core scatterings,}\end{array} \tag{29}$$

where $x_* = 3.26$ is the core–wing transition frequency at $T = 10^4$ K. On the other hand, if the gas remains optically thick far in the wing, Lyα photons primarily escape via diffusion in the frequency space after multiple wing scatterings, that is, via excursion. This escape is dominant in high-$N_{\rm HI}$ channels with (Neufeld 1990; Dijkstra et al. 2006)

$$N_{HI} \gtrsim \frac{10^3}{\sigma_{\alpha,0}a_v} \approx 4 \times 10^{19} \text{ cm}^{-2}, \quad \begin{array}{l}\text{escape via excursion} \\ \text{after wing scatterings,}\end{array} \tag{30}$$

where $a_v = 4.7 \times 10^{-4}$ is the Voigt parameter at $T = 10^4$ K. The resulting Lyα spectrum in the RHD turbulence is therefore controlled by the combination of the above mechanisms.

In summary, the above Lyα transfer mechanism in a turbulent H II region produces diverse Lyα line profiles, including narrow double-peak profiles with high LyC escape fractions. In Figure 11, we show a case that reproduces the observed Lyα profile of a $z \sim 0.3$ LyC-leaking galaxy (J1154 +2443; Izotov et al. 2018a). Although we admittedly chose a simulation that resembles the observation, the match is worth noting, given that the required multiphase structure and the subsequent Lyα transfer naturally emerge from an RHD turbulence simulation representing the H II region in a GMC.

To understand the formation mechanism of Lyα spectra in detail, in Figure 12, we have decomposed three representative
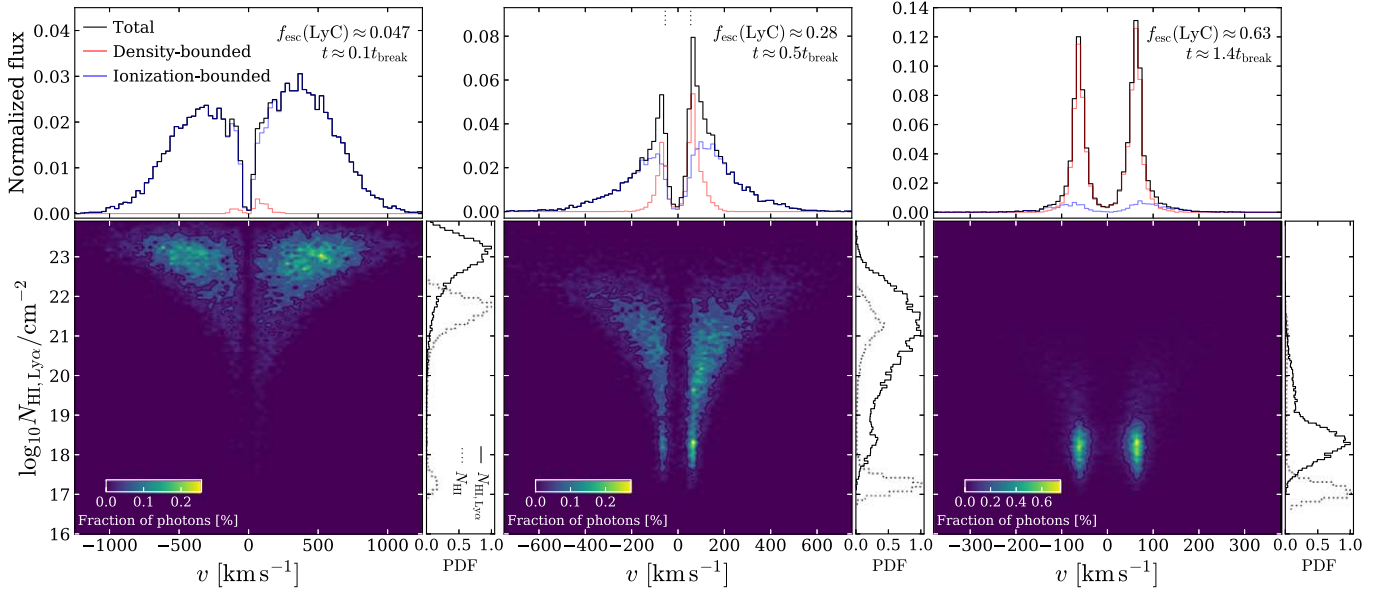
Figure 12. Two-dimensional Lyα spectra decomposed with respect to the total H I column density integrated along the path of a Lyα photon, $N_{\rm HI,Ly\alpha}$. The projection along each axis corresponds to the total Lyα profile (black line, top panels) and the $N_{\rm HI,Ly\alpha}$ PDF (solid line, right panels) normalized at their maximum values. The red and blue lines show the contributions of the photons experiencing $\log_{10} N_{\rm HI,Ly\alpha}/{\rm cm}^{-2} < 20$ and >20, which approximately indicates the photons through photoionized LyC escape channels and optically thick density-bound channels. For reference, a dotted line shows the physical $N_{\rm HI}$ distribution for each snapshot. The spectra are drawn from the V18S_f2e11_RHD simulation at the three different times bracketing the three representative cases (ionization-bound dominated limit, mixed case, and density-bound dominated limit).

Lyα spectra[10] as a function of the integrated H I column density seen by each Lyα photon. Here $N_{\rm HI,Ly\alpha}$ is the H I column density integrated along the path of a Lyα photon. This allows us to quantify the contributions of Lyα photons escaping through various paths to the total Lyα profiles (top panels). Because a Lyα photon travels in a zigzag path through a medium by scattering, its integrated path is longer than the length of the simulation box, leading $N_{\rm HI,Ly\alpha}$ to be generally larger than the physical $N_{\rm HI}$. Figure 12 clearly shows that the two distinct passages of Lyα photons through density- and ionization-bound channels contribute differently to the various components (peaks and broad wings) of the Lyα profile. The origin of each component is detailed below.

5.2. Origin of the Peak Separation

In a LyC-leaking H II region, the Lyα peak separation is determined by the H I column density and temperature of the photoionized LyC escaping channels. Figure 12 shows that when a system shows a high LyC leakage, $f_{\rm esc}^{\rm LyC} \gtrsim 10\%$, the Lyα photons propagating through density-bound channels dominate the location of the Lyα peaks, whereas when there are no or few holes through which LyC photons can escape, a broad peak separation is produced. In the latter case, as the majority of the I-fronts are still bound within a cloud, most of the Lyα photons need to escape by scattering through optically thick, ionization-bound channels of $N_{\rm HI} > 10^{21}$ cm^{-2}. This inevitably leads to a broad Lyα peak separation and low LyC escape fraction. On the other hand, the

formation of a narrow peak separation occurs as soon as the LyC escape channels open up, and Lyα photons can escape through paths of lower column density (Dijkstra et al. 2016a; Eide et al. 2018). As this can happen before the breakout of the average I-fronts, $t < t_{\rm break}$, the separation remains approximately constant even after the breakout ($\Delta v_{\rm peak} \approx 100{-}200\,{\rm km\,s}^{-1}$). This reflects the fact that the peak separation is controlled by the H I column density of the photoionized channels but not by the total averaged H I of the entire medium $\langle N_{\rm HI} \rangle$ (see Figure 7).

The resulting correlation between the peak separation and LyC escape fraction is shown in Figure 13. The simulations show the anticorrelation in agreement with the observed trend (Verhamme et al. 2017; Izotov et al. 2018b). The three representative Lyα spectra (see Figure 12) occupy different regions of the diagram, illustrating how different LyC leakage mechanisms can lead to the Lyα peak separation–LyC escape fraction correlation.

The peak separation of a LyC-leaking H II region can be estimated analytically. Because at the H I column density of the density-bound channels, $N_{\rm HI} \approx 10^{17-18}$ cm^{-2}, the gas is optically thin to the wing, Lyα photons escape freely once the frequency is shifted out of the Doppler core (i.e., via single flight). Therefore, by solving $\tau_\alpha = \tau_{\alpha,0} e^{-x^2} < 1$, we find the escape frequency of $x > \sqrt{\ln \tau_{\alpha,0}}$ (Osterbrock 1962; Zheng & Miralda-Escudé 2002). The peak separation is then estimated by[11]

$$\Delta v_{\rm peak} = 2b \sqrt{\ln \sigma_{\alpha,0} \bar{N}_{HI,{\rm channel}}},$$

$$\simeq 25.6 T_4^{1/2} \sqrt{\ln \left(\frac{\bar{N}_{HI,{\rm channel}}}{1.7 \times 10^{13} T_4^{1/2}\,{\rm cm}^{-2}} \right)}. \qquad (31)$$

---

[10] The Lyα spectra are computed using all Lyα photons escaping in all directions at the outcoming face of the box. The difference between angular- and line of sight–averaged spectra affects the emergent line profiles. For example, if we were to compute the Lyα spectra using only photons escaping along the line of sight of an observer, we would expect that the relative importance of the escape through density-bound channels (which form a narrow Lyα peak separation) would increase, as these photons would more likely escape along the line of sight than those scattered through the high column density regions.

[11] Note that $b_{\rm th} = c_{s,\rm II}$ for hydrogen-only isothermal gas, as assumed in this paper. In general, the thermal velocity $b_{\rm th} \equiv \sqrt{2k_B T/m_H}$ and sound speed $c_s = \sqrt{\gamma k_B T/(\mu m_H)}$ differ, i.e., $b_{\rm th} = \sqrt{2\mu/\gamma}\, c_s$. As we show in Section 5.4, the impact of microturbulence is small, i.e., $b = \sqrt{b_{\rm th} + b_{\rm turb}} \approx b_{\rm th}$. Thus, Equation (31) is a valid estimate for the Lyα peak separation through a turbulent LyC-leaking H II region, as we study in this paper.
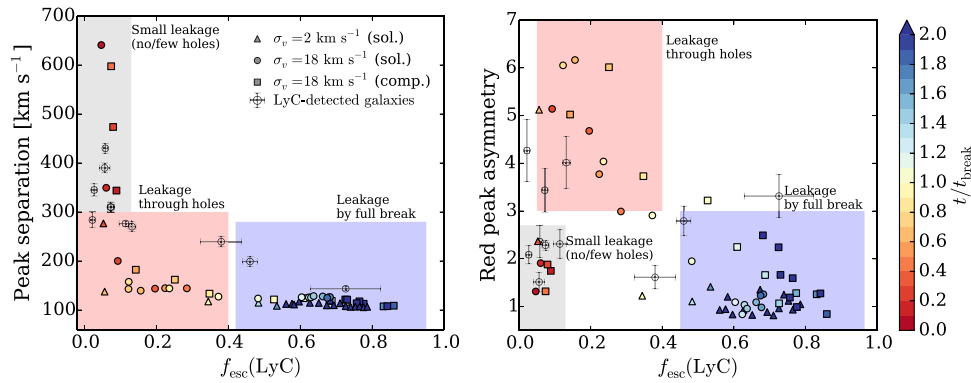
Figure 13. Left: relation between the Lyα peak separation $\Delta v_{\rm peak}$ and LyC escape fraction $f_{\rm esc}^{\rm LyC}$. Right: relation between the Lyα red asymmetry A_f and LyC escape fraction $f_{\rm esc}^{\rm LyC}$. The colors indicate the time normalized by the I-front breakout time of each simulation, $t/t_{\rm break}$, and the different symbols correspond to the three different runs (triangles: V2S_f2e11_RHD; circles: V18S_f2e11_RHD; squares: V18C_f2e11_RHD). The error bars indicate the observed $z \sim 3$ LyC-detected galaxies from Izotov et al. (2016, 2018a, 2018b). The shaded regions are marked to guide the different regimes of LyC leakage and the associated values of the peak separation and asymmetry parameter (see text). The observed outlier at the highest $f_{\rm esc}^{\rm LyC}$ in the right panel is J1243+4646, which in fact shows a triple-peak Lyα line profile. This means that its red peak asymmetry parameter A_f becomes ill-defined. Nonetheless, for completeness, we included this object for comparison.

Evaluating at the values found in the simulation $\bar{N}_{\rm HI,channel} = 2.4 \times 10^{17}$ cm^{-2} and $T = 2 \times 10^4$ K, we find

$$\Delta v_{\rm peak} \approx 110 \text{ km s}^{-1}, \qquad (32)$$

in agreement with the simulated peak separation. Note that, in this case, the peak separation depends weakly on the H I column density of the channels ranging only $\sim$90–120 km s^{-1} over $16 < \log_{10} N_{HI} \text{ cm}^2 < 18$ but more sensitively on the temperature of the channels to nearly $\propto T^{1/2}$ (more precisely, the Doppler b-parameter). The peak separation can vary from $\sim$80 to 235 km s^{-1} over $T = 10^{4-5}$ K ($b = 12.8$–40.5 km s^{-1}). This is a direct consequence of the Doppler core scattering. As a corollary, it is possible that the leakage of hot gas through the channels in the H II regions (Lopez et al. 2011, 2014) elevates the Lyα peak separation. This contrasts with the estimate $\Delta v_{\rm peak} \simeq 300 T_4^{1/6}(N_{H I}/10^{20}\text{cm}^{-2})^{1/3}$ km s^{-1} for $N_{\rm HI} \gtrsim 10^{18}$ cm^{-2} (e.g., Adams 1972; Dijkstra 2017), where the peak separation depends mostly on the H I column density. This regime is only valid when Lyα photons escape via excursion and thus only applies to an ionization-bound dominated system with high H I coverage in nearly all directions. This dichotomy is in accordance with the Monte Carlo calculation of Verhamme et al. (2015), where the peak separation of a homogeneous shell spans these two regimes depending on the H I column densities.

The fact that the Lyα peak separation of a high LyC-leaking medium reflects the H I column density of the escape channels instead of the average H I of the system has an observational implication. Abundant H I gas of mass $M_{\rm HI} \sim 10^{7-9} M_\odot$ in blue compact dwarf galaxies (Thuan et al. 2016; McKinney et al. 2019) and the LARS sample selected to be comparable to high-z LAEs and LBGs (Pardy et al. 2014, 2016; Puschnig et al. 2017) is revealed by 21 cm observations. This corresponds to the average H I column density of $\langle N_{HI} \rangle \sim 5 \times 10^{19}$ cm$^{-2}(M_{\rm HI}/10^7 M_\odot)(R/5 \text{ kpc})^{-2}$. At face value, this seems to exceed the value that allows narrow Lyα peak separation and high LyC leakage. This, however, can be explained if a galaxy consists of an ensemble of LyC-leaking H II regions that are multiphase, for example, those generated by RHD turbulence. In such a system, while the Lyα peak separation and LyC leakage are regulated by the escape of the

photons through low column density channels, the majority of H I still resides in the neutral phase, keeping the average H I column density of the system high, as observed by the 21 cm line. Similar arguments may apply for the high H I coverage found in gamma-ray burst host galaxies (Tanvir et al. 2019). However, as both the covering fraction and the derived column density depend on the modeling of the absorption lines, we defer a detailed comparison to future work.

5.3. Origin of the Peak Asymmetry

The Lyα peak asymmetry also reflects the multiphase nature of the turbulent H II regions. When Lyα escapes, some of the Lyα photons need to undergo multiple scattering events through optically thick channels before the complete I-front breakout occurs. These photons diffuse more in frequency space and produce a broad wing component ($|v| \gtrsim 250$ km s^{-1}) of the emergent Lyα profile. This component is clearly seen in Figure 12 when the optically thick ionization-bound channels exist.

The presence of multiple routes of Lyα escape can be quantified by the asymmetry parameter of the red Lyα peak, A_f, defined as the ratio of the blue-to-red flux of the red peak,

$$A_f = \frac{\int_{\lambda_{\rm peak}^{\rm red}}^{\infty} f_\lambda \, d\lambda}{\int_{\lambda_{\rm valley}}^{\lambda_{\rm peak}^{\rm red}} f_\lambda \, d\lambda}, \qquad (33)$$

where f_λ is the flux, $\lambda_{\rm peak}^{\rm red}$ is the wavelength at the red peak, and $\lambda_{\rm valley}$ is the wavelength at the minimum between the red and blue peaks. This is similar to the asymmetry statistics introduced by Rhoads et al. (2003). Figure 13 shows the relation between the red peak asymmetry parameter and LyC escape fraction. The shaded regions in the diagram mark the approximate regions occupied by the different LyC leakage mechanisms (associated with the three representative Lyα spectra shown in Figure 12). The simulations indicate that the Lyα peak asymmetry is high ($A_f \gtrsim 3$) when both optically thin and thick channels coexist, whereas the asymmetry is low ($A_f \lesssim 3$) when the medium is dominated either by ionization- or density-bound channels, in which only one type of Lyα escape is possible (either via single flight or excursion). This means that the anisotropic LyC leakage through holes in a

turbulent H II region and isotropic LyC leakage from a fully density-bound H II region can be distinguishable by measurement of the peak asymmetry. While both mechanisms allow a high LyC escape fraction $f_{esc}^{LyC} \gtrsim 10\%$, the former favors a high asymmetry parameter ($A_f \gtrsim 3$), whereas the latter is associated with a low asymmetry parameter ($A_f \lesssim 3$).

We have measured the red peak asymmetry parameter using the archival COS Lyα spectra of the $z \sim 0.3$ LyC-detected sample of Izotov et al. (2016, 2018a, 2018b; see Appendix B). Comparison with the simulation suggests that there may be a tentative trend indicating various LyC leakage mechanisms in the observed LyC-detected galaxies. A detailed analysis of the individual objects with the synthetic H II regions is needed to confirm the trend.

5.4. Role of Outflow and Turbulence on the Lyα Line

In order to examine the effect of kinematics on the Lyα line profile, Figure 14 compares the two sets of Monte Carlo Lyα RT simulations with and without the velocity fields from the RHD turbulence.

The outflow driven by the photoionization heating (and radiation pressure) produces the enhancement of the red peak relative to the blue peak. An effect of outflow on the line profile is well known (e.g., Dijkstra et al. 2006; Verhamme et al. 2006). Here the enhancement is modest, as the outflow velocity $\langle v \rangle_{outflow}$ is only a few tens of km s^{-1}, approximately corresponding to the expansion velocity of the I-front. Note that our RHD turbulence simulations show a double-peaked profile because the outflow velocity of the photoionized channel is

$$\langle v \rangle_{outflow} < b\sqrt{\ln \sigma_{\alpha,0}\bar{N}_{H\,I,channel}}, \tag{34}$$

where $b\sqrt{\ln \sigma_{\alpha,0}\bar{N}_{H\,I,channel}} \approx 40T_4^{1/2}$ km s^{-1} at $\bar{N}_{H\,I,channel} = 2.4 \times 10^{17}$ cm^{-2} ($b \approx c_{s,II}$; see below). At this modest outflow velocity, the gas remains optically thick to the Lyα photons emitted at line center. Therefore, the photons will be absorbed and undergo core scattering before escape. On the other hand, if the outflow velocity becomes faster, such that $\langle v \rangle_{outflow} > b\sqrt{\ln \sigma_{\alpha,0}\bar{N}_{H\,I,channel}}$, the photoionized channels are no longer optically thick to the photons emitted at line center, which can now freely escape with fewer interactions. Therefore, we expect that if the photoionized gas is accelerated further by other (stellar) feedback, the emergent Lyα profile will show a single peak component with a large Lyα flux at line center.

In Figure 14, the effect of turbulent velocities on the peak separation appears small. This is somewhat surprising, as the naïve inclusion of the turbulence via a simple rescaling of the Doppler b-parameter, $\Delta v_{peak} \propto b = c_{s,II}\sqrt{1 + \mathcal{M}_{II}^2}$, suggests an $\sim 50\%$ increase in the peak separation ($\sqrt{1 + \mathcal{M}_{II}^2} = 1.49$ at $\mathcal{M}_{II} \approx 1.1$ for the fiducial run), which is not observed in the simulation. To understand correctly, we need to note that core scattering of Lyα photons happens on a small scale of the order of the mean free path $\lambda_{mfp}^{core} = 1/(\sigma_{\alpha,0}n_{HI})$ or in units of the length of the slab $\lambda_{mfp}^{core}/L = 1/\tau_{\alpha,0}$. On the other hand, the rms Mach number refers to the turbulent velocity dispersion measured at the driving scale, i.e., at the length scale of slab L. The turbulent cascade transfers energy from large to small scales, with the velocity dispersion decreasing to smaller scales.
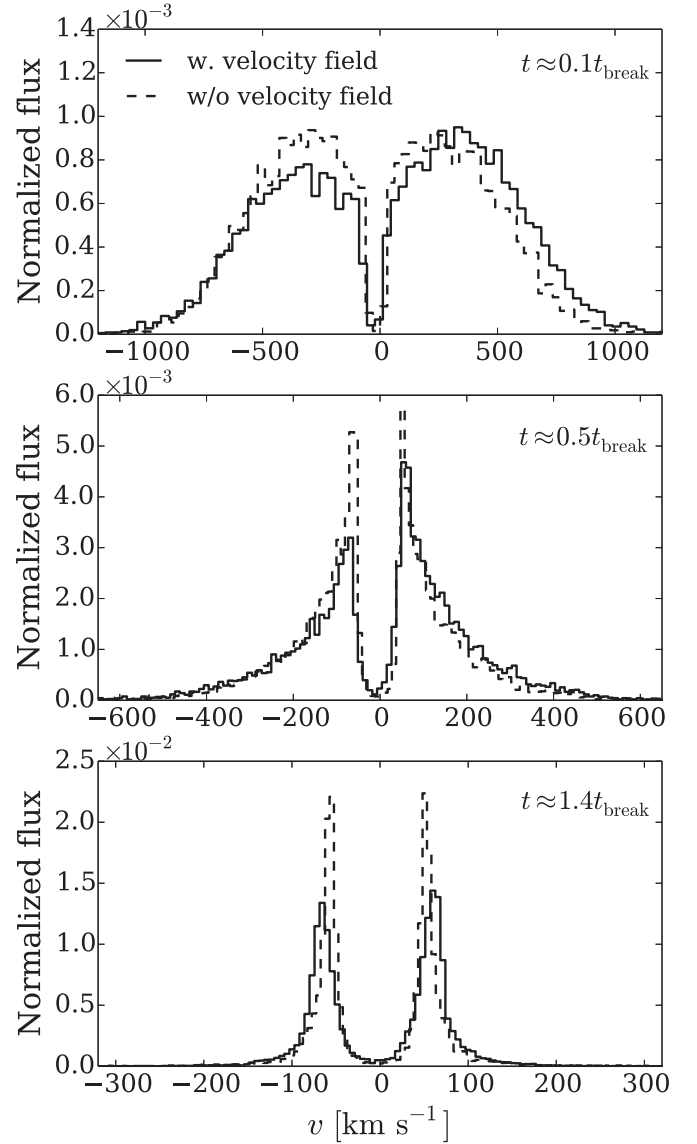

Figure 14. Influence of the gas kinematics of the H II region on the Lyα line profile. The Lyα spectra from the Monte Carlo Lyα simulations based on `V18S_f2e11_RHD` with (solid) and without (dashed) the velocity field are shown for the three representative snapshots.

The velocity dispersion at the length scale ℓ is

$$\sigma_v(\ell) = c_{s,II}\left(\frac{\ell}{\ell_s}\right)^{\beta}, \tag{35}$$

where ℓ_s is the sonic length and $\beta > 0$ is the scaling exponent (e.g., $\beta = (n-1)/2$, where n is the power-law index of the velocity power spectrum $P_v(k) \propto k^{-n}$ and $n = 5/3$ for subsonic and 2 for supersonic turbulence; see Krumholz 2014 for a review). Therefore, the velocity dispersion at the scale of the core mean free path is

$$\sigma_v(\lambda_{mfp}^{core}) \sim c_{s,II}\mathcal{M}_{II}\tau_{\alpha,0}^{-\beta}. \tag{36}$$

Thus, we argue that more appropriate inclusion of turbulence on the Doppler b-parameter is

$$b = c_{s,II}\sqrt{1 + \mathcal{M}_{II}^2\tau_{\alpha,0}^{-2\beta}} \approx c_{s,II}. \tag{37}$$

As $\tau_{\alpha,0} \sim 10^4$ along the photoionized channels, the turbulent velocity dispersion becomes negligibly small due to the turbulence cascade to the small scale of core scattering.[12] Thus, to first order, the effect of turbulence on the peak separation remains small. A more precise estimate would defer from this, as the turbulent velocity field is spatially correlated. We do not examine the precise influence of turbulence on spectral lines (Mihalas 1978; Silant'ev et al. 2006), which may become increasingly important for a highly supersonic H II region ($\mathcal{M}_{\mathrm{II}} \gg 1$).

5.5. Shocked H I Shell and Fermi Acceleration?

We end by discussing the formation and destruction of the H I shell upon the propagation of the D-type I-front and the influence on the Lyα profile. In a homogeneous medium, the D-type I-front creates a shell of neutral hydrogen by the propagation of the photoheated shock front at the boundary of the H II region (Whalen et al. 2004; Hosokawa & Inutsuka 2006), providing a probable mechanism for the classic shell model of Lyα RT. However, in a turbulent medium, this H I shell is constantly perturbed by the turbulent flow as the I-front shock propagates through the system, making its fate unclear.

Figure 15 shows the structure across the I-front for different turbulent velocities, indicating that an H I shell-like structure is disturbed for increasing turbulence. As the velocity of the shocked shell is of the order of the sound speed $v_{\mathrm{sh}} \sim c_{s,\mathrm{II}} \simeq 12.8 T_4^{1/2}$ km s^{-1}, with increasing turbulent velocities, the timescale of the supersonic turbulent mixing becomes comparable to or faster than the speed that the I-front shock sweeps up the neutral material, $\sigma_v > v_{\mathrm{sh}}$. This causes the I-front shock to be constantly destroyed and mixed up with the neutral turbulent gas ahead of the I-front as soon as the H I shell develops. The simulations indicate that this is the case, and the H I shell is not formed for a higher Mach number. For a lower Mach number, the remnant of the shell structure is still visible and would survive on the order of the Eddy turnover timescale.

This dispersal of the H I shell and the small shock velocity limit the efficiency of blue wing and bump production via Fermi-like acceleration of Lyα photons across shock fronts (Neufeld & McKee 1988; Chung et al. 2016). In principle, the Fermi-accelerated Lyα contributes to blueshifted components at $\sim n v_{\mathrm{sh}}$ after n crossings of a shock front (Chung et al. 2016). However, as the shock velocity of the D-type I-front is small, even after several shock crossings, the Fermi-accelerated Lyα photons only gain blueshifts of ~ 25–80 km s^{-1}. The gas outside the H II region is optically thick to these blueshifted photons with high column densities of $N_{\mathrm{HI}} > 10^{21}$ cm^{-2}. Therefore, the substantial frequency space diffusion of several hundreds of km s^{-1} occurs by subsequent scattering through the ambient H I gas, effectively erasing the blueshifted component by the Fermi acceleration. In fact, Neufeld & McKee (1988) estimated that for the Fermi-accelerated blue peak to exceed the typical frequency diffusion of a slab, the shock velocity needs to exceed $v_{\mathrm{sh}} > 40 T_4^{1/2}$ km s^{-1}. This

---

[12] We have provided a physical argument. Clearly, we do not resolve the full cascade down to the scale of the mean free path in the simulation. Instead, it is limited to the grid scale of the simulation. However, the velocity dispersion becomes much smaller than the sound speed, even after limiting the calculation to only the grid scale.
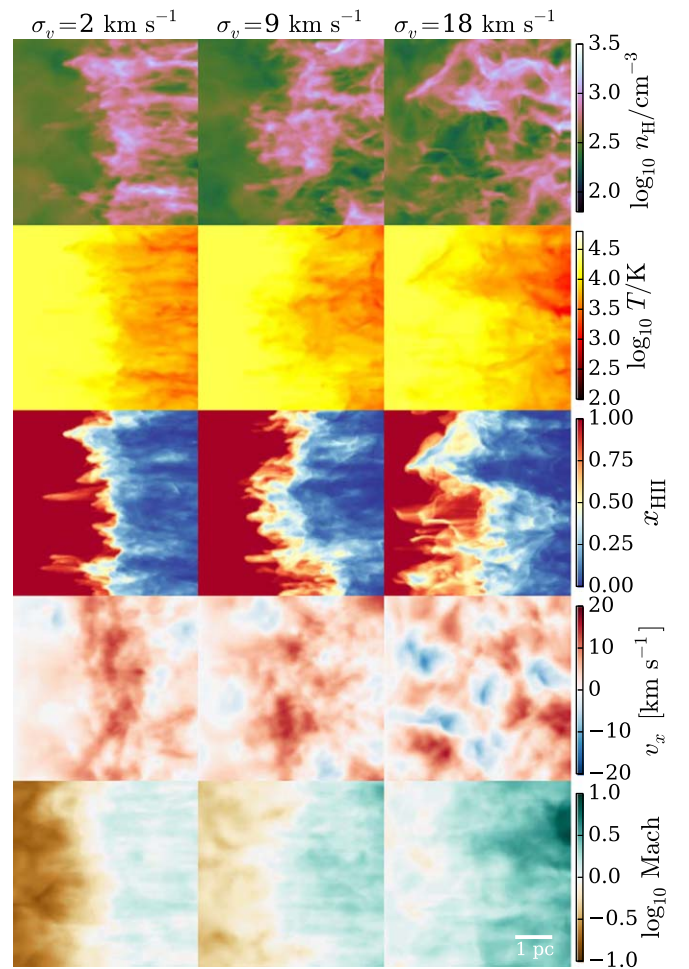

Figure 15. Formation and destruction of the shocked H I shell in a turbulent medium. Projected maps of gas density n_{H}, mass-weighted temperature T, ionized fraction x_{HII}, x-velocity v_x, and the Mach number of the local rms velocity dispersion for the three simulations with different turbulent velocities (left: `V2S_f2e11_RHD`; middle: `V9S_f2e11_RHD`; right: `V18S_f2e11_RHD`) are shown. All snapshots are at 0.10 Myr.

value is hard to satisfy with the shock generated by the D-type I-front. Indeed, all of our simulations show no noticeable effect of Fermi acceleration on the emergent Lyα profile. We expect that, in order for the production of Fermi-accelerated blue wings and bumps to be effective, other forms of feedback, such as a supernova blast wave or stellar winds in the H II region, are required to accelerate the shocked H I shell to several hundreds of kilometers per second before being destroyed by turbulence.

6. Discussion

6.1. Missing Physics: Dust

We have employed an idealized RHD turbulence simulation in order to study the development of I-fronts and the associated LyC leakage and the Lyα line. We have ignored the effect of dust, metal line cooling, stellar winds, and gravity, as well as the hydrodynamic instabilities associated with these missing physical processes. Here we discuss the limitations of our simulations and caveats.

Following the simple model assuming dust is perfectly mixed with gas, we find that the dust cross section per hydrogen atom

is well approximated by $\sigma_{\rm dust}(\lambda) \simeq 5.3 \times 10^{-22}$ $(\lambda/912~\mathring{\rm A})^{-1}$ $(Z/0.25\,Z_\odot)$ cm^2 H^{-1} over $800\,\mathring{\rm A} < \lambda < 1500\,\mathring{\rm A}$ (Gnedin et al. 2008).[13] The dust cross section is 4 orders of magnitude lower than the photoionization cross section. In photoionized channels, however, as the optical depth at the Lyman limit is $\tau_L = \sigma_L N_{\rm H I}[1 + \sigma_{\rm dust} N_{\rm H}/(\sigma_L N_{H1})]$, where $\sigma_{\rm dust} N_{\rm H}/(\sigma_L N_{H1}) = 0.84(Z/0.25\,Z_\odot)(x_{\rm HI}/10^{-4})^{-1}$, the dust extinction can become comparable to the absorption by photoionization. For a system with a metallicity higher than $Z \geqslant 0.3(x_{\rm HI}/10^{-4})Z_\odot$, LyC leakage becomes increasingly suppressed by the absorption by dust. Strictly speaking, our idealized RHD turbulence simulation should therefore only be applicable for a metal-poor system with $Z \ll 0.3(x_{\rm HI}/10^{-4})\,Z_\odot$, where dust extinction becomes negligible.[14] Furthermore, there is observational evidence that the dust-to-gas ratio may drop more rapidly than the linear extrapolation $\sigma_{\rm dust} \propto Z$ assumed here, below $12 + \log{\rm O/H} \leqslant 8$ (Rémy-Ruyer et al. 2014). As we are concerned with metal-poor LyC-leaking systems ($12 + \log{\rm O/H} \lesssim 8$, i.e., $Z = 0.2\,Z_\odot$; Izotov et al. 2016, 2018b) and those analogous to reionization-era galaxies (Nakajima et al. 2016; Senchyna et al. 2017), this condition is reasonably met. Therefore, our conclusion should be minimally affected by the complication by dust.

However, the effect of dust on the Lyα line properties can be complex. The abundance and distribution of dust controls the Lyα escape fraction (Neufeld 1990). Furthermore, dust can also affect the Lyα line shape, as the level of dust attenuation is usually a function of the emergent frequency (Neufeld 1990; Laursen et al. 2009). In the case where the dust is perfectly mixed with the neutral hydrogen, for instance, photons with an overall longer trajectory are more prone to destruction by dust. This can lead to an increased global asymmetry of the emergent spectrum; e.g., in the context of a homogeneous shell or slab, the dust content can change the ratio of the peak fluxes for a double-peaked profile (e.g., Gronke et al. 2015). For similar reasons, increased dust content will make the individual peaks narrower (as photons further in the wing had a longer path length through neutral hydrogen and are thus more prone to destruction). This implies that the red peak asymmetry defined in Section 5.3 will be lowered in such a scenario. However, while in Lyα RT studies, it is frequently assumed that the dust number density is proportional to the neutral hydrogen, dust creation and destruction mechanisms likely lead to a (Lyα-affecting) dust distribution that is far more complex than this. For instance, dust may survive in ionized regions (given that they are not too hot), or it clumps on small scales due to streaming instabilities. Therefore, we leave the study of the imprint of dust on the Lyα–LyC connection for future work.

6.2. Missing Physics: Metal Cooling, Winds, and Hydrodynamic Instabilities

Metal line cooling introduces an interesting complication to the problem. If the neutral shocked shell ahead of the D-type I-front can radiatively cool by metal lines, the shocked gas is prone to fragmentation via a so-called *thin-shell instability* (Whalen & Norman 2011, and references therein). This facilitates the formation of cracks in the shell and allows further escape of radiation through the channels. The growth of the thin-shell instability depends on the availability of efficient cooling mechanisms beyond primordial hydrogen and helium cooling (Whalen & Norman 2008a, 2008b). Since we have ignored the effect of cooling by metal lines, this mode of instability is inhibited by design.

There are other instabilities and winds that may influence the structure of the H II region. Under a gravitational field, the Rayleigh–Taylor instability can also develop as rarefied ionized gas pushes the dense ambient neutral medium (e.g., Jacquet & Krumholz 2011; Jiang et al. 2013; Park et al. 2014), which, if operating on the relevant timescales, can further contribute to the fluctuation of the I-fronts. The metal line–driven stellar winds of massive stars can inject fast outflows into the H II region, which can produce hot X-ray-emitting gas of $\sim 10^6$ K by clumping and shocks in the outflowing gas amplified by the line-deshadowing instability (e.g., Owocki 2015). The wind-blown bubble can further evacuate the gas through openings of low column density channels, in which both hot gas and radiation can leak out more efficiently (Rogers & Pittard 2013). Again, this will likely amplify fluctuations in the I-fronts and multiphase structure of H II regions initially seeded by turbulence. Inclusion of metal line cooling, stellar winds, and gravity would therefore lead to the amplification of the I-front inhomogeneities, probably allowing more escape of radiation, and alter the emergent Lyα spectra. However, as we have studied the development of the I-front in a driven turbulence medium, the growth of the instabilities is subject to constant destruction by external turbulent mixing over the Eddy turnover timescale. Thus, it still remains unclear what the exact impact of the instabilities and winds under an external source of turbulence are and how they ultimately influence the LyC leakage and Lyα spectra.

6.3. Influence of Turbulence on Other Nebular Lines

The intense nebular [O III]+Hβ and He II emission lines are often associated characteristics of reionization-era and LyC-leaking galaxies. As discussed in Section 4, supersonic turbulence in the H II region can induce density fluctuations. Since the nebular recombination lines scale as $\propto n_e^2$, this may lead to enhanced nebular emission line luminosity,

$$L_{\rm neb} = \gamma_{\rm neb}(T)\bar{n}_e^2 \mathcal{C}(\mathcal{M}_{\rm II}) V_{\rm HII}$$
$$\approx \gamma_{\rm neb}(T)\bar{n}_e^2 \left[1 + \left(\frac{\mathcal{M}_{\rm II}}{3}\right)^2\right] V_{\rm HII}, \qquad (38)$$

where $\gamma_{\rm neb}(T)$ is the emission coefficient and $V_{\rm HII}$ is the volume of the H II region. For example, a high velocity dispersion medium with $\mathcal{M}_{\rm II} = 3$ (i.e., $\sigma_v \approx 38$ km s^{-1}) could lead to a factor of 2 boost in the emission line luminosity. The equivalent width of the emission line could also be boosted accordingly.

Gray & Scannapieco (2017) examined the impact of turbulence on the line ratios in detail by incorporating the nonequilibrium chemistry. They showed that a high turbulent velocity generally increases the nebular emission line ratios due to the associated temperature fluctuations, which mimic the

---

[13] This is based on a fit of Gnedin et al. (2008) to Weingartner & Draine (2001) for SMC-type dust, assuming a linear dust-to-gas ratio $\propto Z$ normalized at the gas-phase metallicity of the SMC, $Z = 0.25\,Z_\odot$ ($12 + \log{\rm O/H} = 8.1$; Pagel 2003). Note that in reality, a fraction of the dust is likely destroyed in the hot, ionized channels, and therefore this estimate overpredicts the impact of dust on the LyC leakage.

[14] At $Z = 0.1\,Z_\odot$, if we reestimate $f_{\rm esc}^{\rm LyC}$ from our fiducial simulation after adding the optical depth from dust, the value reduces by about a factor of 2. At $Z < 0.05\,Z_\odot$, the effect of dust on $f_{\rm esc}^{\rm LyC}$ decreases below 50%.

effect of harder stellar sources in the locus of nebular diagnostic diagrams. Because we have neglected metals and assumed an isothermal equation of state, this effect is missing from our simulations. The clumping and thermal fluctuations may complicate the relation between LyC escape fractions and [O III]/[O II] ratios (Faisst 2016; Izotov et al. 2016) and contribute to the observed scatter in the $f_{esc}^{LyC} - $ [O III]/[O II] correlation (Naidu et al. 2018; Bassett et al. 2019).

For Lyα line profiles of green pea galaxies, when interpreted with homogeneous shell models, the required intrinsic Lyα line width exceeds that of the observed Hβ line width ($\sim$130–230 km s^{-1}) for successful fit to the data, which causes problematic fits when consistency with Hα, Hβ, and/or [O III] λ5007 line widths is required (Yang et al. 2016, 2017; Orlitová et al. 2018, but see Gronke et al. 2018). For a turbulent H II region, a narrow Lyα injection at line center can produce both a narrow peak separation through photoionized channels and a broad wing component by multiple scatterings through optically thick channels. As the turbulence line broadening of the ionized gas is of the order of tens of km s^{-1}, the observed Hβ line width can still accommodate the turbulence broadening within individual H II regions, as well as the contributions from thermal broadening and the velocity dispersion of multiple H II regions in a galaxy.

Overall, it is important to include the effect of turbulent H II regions on the nebular emission lines in stellar + H II region population synthesis modeling to understand the observed relations between LyC, Lyα, and nebular emission line properties.

6.4. Scale of LyC Leakage: Observational Test with the Magellanic Systems and Local Blue Compact Dwarfs

The picture that LyC leakage from the ISM of a galaxy is controlled by the escape fractions through molecular clouds assumes that a major source of opacity in the ISM comes from GMCs rather than diffuse gas in between them, arguing that the galactic escape fraction averaged over an entire galaxy is approximated as $f_{esc,gal}^{LyC} \approx \langle f_{esc,GMC}^{LyC} \rangle$,

$$\langle f_{esc,GMC}^{LyC} \rangle \equiv \frac{\int \dot{N}_{ion}(M_{cl}) f_{esc}^{LyC}(M_{cl}) \frac{d\mathcal{N}}{dM_{cl}} dM_{cl}}{\int \dot{N}_{ion}(M_{cl}) \frac{d\mathcal{N}}{dM_{cl}} dM_{cl}}, \qquad (39)$$

where $f_{esc,gal}^{LyC}$ is the galactic escape fraction that is averaged over an entire galaxy, $f_{esc}^{LyC}(M_{cl})$ is the escape fraction from a GMC of mass M_{cl}, and $d\mathcal{N}/dM_{cl}$ is the mass distribution of the GMCs. We discuss a way to test the spatial scale responsible for LyC leakage and the associated feedback in the H II regions.

The galactic escape fraction can be inferred from the diffuse Hα emission from the CGM of a galaxy (Bland-Hawthorn & Maloney 1999; Mas-Ribas et al. 2017). This approach has been applied to the two local dwarf galaxies, the Small Magellanic Cloud (SMC) and LMC, of the Milky Way by Barger et al. (2013). They found that the diffuse Hα emission from the Magellanic Bridge—the diffuse gas in between the Magellanic Clouds—shows an excess Hα surface brightness from the diffuse gas that cannot be explained by the photoionization from the escaping ionizing radiation from the Milky Way (a few percent $f_{esc,gal}^{LyC}$; Bland-Hawthorn & Maloney 1999, 2001) and the extragalactic UV background (Haardt & Madau 2001). By attributing the Hα emission to the photoionization due to the LyC photons leaking from the Magellanic Clouds, they

placed upper limits on the escape fraction of $f_{esc,gal}^{LyC} < 4.0\%$ for the LMC and $f_{esc,gal}^{LyC} < 5.5\%$ for the SMC. As this measures the LyC photons arriving at the Magellanic Bridge after escaping the Magellanic Clouds, it provides a measure of the "galactic" escape fraction.

On the other hand, escape fractions from individual H II regions in a galaxy can be measured by estimating the direct ionizing photon production rate of the massive stars (by direct stellar spectroscopy or spectral energy distribution fitting) and the recombination rate in each H II region. As the nebular Hα luminosity of the H II region is proportional to the amount of ionizing photons absorbed (recombined) in the region, each escape fraction can be estimated by $f_{esc,GMC}^{LyC} = 1 - \dot{N}_{rec}/\dot{N}_{ion}$. The application of the method to the LMC indicates that the brightest H II region, 30 Doradus, has an escape fraction of $f_{esc,GMC}^{LyC} \sim 6_{-6}^{+55}\%$ (Doran et al. 2013). An individual H II region's escape fraction varies enormously from object to object; for example, the H II region complexes N44 and N180 show escape fractions as large as $f_{esc,GMC}^{LyC} \sim 40\%$–80% (McLeod et al. 2019). Each H II region can be classified via line ratios to ionization- or density-bound nebula using ionization parameter mapping, and, when the indirect measurement of $f_{esc,GMC}^{LyC}$ is averaged over all H II regions, it has been suggested that the population-averaged escape fraction is $\langle f_{esc,GMC}^{LyC} \rangle \sim 42\%$ for the LMC (Pellegrini et al. 2012).

If this value of $\langle f_{esc,GMC}^{LyC} \rangle$ is compared to the estimate of $f_{esc,gal}^{LyC}$, at face value, it seems that the additional $\sim$90% of LyC absorption by the diffuse ISM between the H II regions is required to give the observed galactic escape fraction. Unfortunately, the uncertainties, including the recently revised extragalactic UV background value (e.g., Shull et al. 2015; Khaire et al. 2019) and various differing assumptions, make it difficult to draw a definitive conclusion. The above argument nonetheless should illustrate a way in which the mechanism of LyC leakage could be tested observationally. Given the similarity of the central star-forming region NGC 2070 of 30 Doradus to the local LyC-leaking and green pea galaxies in their emission line and star formation properties (Crowther et al. 2017), the modern integral field spectroscopic census of H II regions of the Magellanic Clouds and the revised homogeneous analysis of $f_{esc,GMC}^{LyC}$ and $f_{esc,gal}^{LyC}$ will be extremely useful to examine the physical mechanism and scale of LyC leakage. Such an analysis will also allow the system's LyC leakage to be correlated with the stellar feedback mechanisms in the H II regions, including photoionization heating, radiation pressure, and stellar winds by massive stars (Lopez et al. 2011, 2014; McLeod et al. 2019).

A similar method should be applicable for nearby blue compact dwarf galaxies for which the individual H II regions and the diffuse Hα emission from the halos may be examined by narrowband imaging and/or deep integral field spectroscopy. The closely related approach was already taken by Weilbacher et al. (2018), who examined the LyC leakage from the H II regions in the Antennae galaxy, and Menacho et al. (2019), who reported the diffuse Hα halo around a LyC-leaking galaxy, Haro 11. Such observational samples should provide valuable spatially resolved reference samples for reionization-era galaxies to test the role of turbulence and stellar feedback on LyC leakage and help the interpretation of future observations with the JWST and Extremely Large Telescopes (ELTs).

7. Conclusions

We have examined the physical origin of LyC leakage and the associated Lyα spectra through turbulent H II regions using fully coupled RHD simulations representing the growth of the I-front in a GMC. Using a series of RHD turbulence simulations with RAMSES-RT in a plane-parallel geometry where the turbulence is constantly driven on parsec scales, we have computed LyC escape fractions and calculated the associated Lyα spectra using the Monte Carlo RT code TLAC, whereby their correlations with H I covering fractions, gas kinematics, and ionizing photon production efficiency and the roles of turbulence and radiative feedback were examined in detail.

We find that LyC photons escape through turbulence-generated low column density channels in an H II region that is evacuated efficiently by radiative feedback induced by shocks due to photoionization heating across the D-type I-fronts. Both turbulence and radiative feedback are key ingredients for regulating the LyC leakage. Because both processes can operate just after the birth of massive stars, high LyC leakage can be achieved at early times, before the onset of supernova feedback. This mechanism generates a time-variable LyC escape fraction that anticorrelates with the H I covering fraction and correlates with the turbulence velocities and ionizing photon production efficiency of the sources. As the LyC photons recombine through the low column density channels, the resulting escape fraction deviates from the $1 - f_{\rm cov}$ expectation. This confirms that while a low H I covering fraction is a necessary condition for high LyC leakage, it only provides an upper limit to the actual escape fraction. The turbulent gas kinematics influences the escape fraction by modifying the densities through the photoionized channels, which generally lead to increasing escape fractions with higher turbulence velocities at a given H I covering fraction and ionizing photon production efficiency.

The emergent Lyα spectra correlate with the LyC leakage mechanism, reflecting the porosity and multiphase structure of the turbulent H II regions. The Lyα photons funnel through the photoionized channels in which LyC photons escape. Depending on the availability of the ionization- and density-bound channels, which are regulated by turbulence and radiative feedback, the H II regions produce diverse Lyα spectral morphology, including narrow double-peaked profiles. For a LyC-leaking H II region, instead of the total H I column density of the system, the Lyα peak separation is set by the residual H I column density and temperature of the photoionized channels. This means that it is possible to have a system with narrow Lyα peak separation and high LyC leakage while retaining a relatively high H I mass, on average. The peak asymmetry reflects the porosity of the H II region. A low asymmetry is often associated with both density- and ionization-bound dominated systems, whereas a high asymmetry is associated with a mixed system of the two phases, as multiple routes of Lyα escape are available. It may therefore be possible to distinguish anisotropic LyC leakage through holes and isotropic leakage from a fully density-bound medium using the red peak asymmetry as a diagnostic.

In summary, radiative feedback through LyC-leaking H II regions in turbulent molecular clouds provides an appealing picture to interpret the observed Lyα spectra of LyC-leaking galaxies and a natural mechanism to explain some of the observed Lyα spectral characteristics. This general picture is in agreement with what is found in the molecular cloud simulations by Kimm et al. (2019).[15] This provides an appealing hypothesis to explain the high LyC leakage and Lyα spectra observed in very young star-forming galaxies in the local universe without need of extreme galactic outflows or supernova feedback. Although the diffuse ISM and CGM will clearly add additional complexities to the observed LyC leakage and Lyα spectral properties, it is worth emphasizing the importance of the physical processes in H II regions and GMCs that are poorly resolved components in galaxy formation simulations and often treated only in a simplified manner in the stellar population synthesis tools and photo-ionization modeling used for the analysis of observed galaxies.

The connection between turbulence and stellar feedback in H II regions, LyC leakage, Lyα spectra, and nebular emission lines is testable with integral field spectroscopic studies of blue compact dwarf galaxies and the H II regions in the Magellanic Clouds. These targets represent valuable laboratories for reionization-era systems. In order to correctly interpret the upcoming JWST and ELT observations of high-redshift galaxies, it is critical to incorporate the impact of turbulent H II regions and the associated LyC, Lyα, and rest-frame UV-to-optical line properties self-consistently in the stellar population synthesis modeling. Further theoretical and observational investigations are needed. Future prospects include providing a spectral library of H II regions using RHD simulations for population synthesis and calibrating against the spatially resolved studies of H II regions and nearby dwarfs as analogs of reionization-era galaxies.

---

[15] The major difference arises from the difference between the numerical diffusivity in the RT solver and driven vs. decaying turbulence in our and Kimm et al.'s simulations. Kimm et al. used the GLF solver, while we used the HLL solver for RT. This means that our simulation creates more "spiky" ionized low column density channels by the shadowing effect than their simulation. Also, our driven turbulence setup produces more channels and I-front fluctuations than their decaying turbulence setup. This difference in the simulated H II region structure translates to the difference in the emergent Lyα line profile. For example, in their simulation, the peak separation jumps from large values (i.e., at the limit of Lyα escape by excursion to the wing) to small values (i.e., at the limit of escape via single flight after core scattering) as their weakly fluctuated I-front breaks out from the cloud almost simultaneously, and therefore the LyC escape fraction suddenly jumps to near unity. On the other hand, our transition of the peak separations as a function of LyC escape fractions is more gradual because our higher level of I-front fluctuations allows more gradual LyC escape.

Appendix A
Turbulence Forcing Method

We implemented the turbulence forcing scheme to RAMSES-RT to enable the fully coupled RHD simulations of a driven turbulence medium. In our implementation, we perturb the momentum and gas energy density 10 times per eddy turnover timescale $T = L/(2V_{\rm rms})$, where $V_{\rm rms}$ is a simulation parameter. Each update is given by

$$(\rho \boldsymbol{v})^{n+1} = (\rho \boldsymbol{v})^n + \rho^n \delta \boldsymbol{v}, \tag{40}$$

$$E^{n+1} = U^n + \frac{1}{2}(\rho \boldsymbol{v} \cdot \boldsymbol{v})^{n+1}, \tag{41}$$

where $\delta \boldsymbol{v}$ is a Gaussian random field and U is the internal energy. We have chosen this reduced frequency of the turbulence forcing update scheme to reduce the computational cost. We generated the velocity perturbation field using two different methods.

The first method is the one used by Robertson & Goldreich (2012, 2018), which is, in turn, based on Kritsuk et al. (2007). The random velocity perturbation field is generated by

$$\delta \tilde{\boldsymbol{v}}(\boldsymbol{k}) = \hat{\sigma}_v(\boldsymbol{k}) \boldsymbol{P}_\zeta(\boldsymbol{k}) \boldsymbol{n}(\boldsymbol{k}), \tag{42}$$

where $\boldsymbol{n}(\boldsymbol{k})$ is the Fourier transform of a white-noise field, and $\hat{\sigma}_v(\boldsymbol{k})$ is the injection power spectrum, for which we choose a flat spectrum over $1 < k < k_0$ but is otherwise zero. The normalization of the injection spectrum is chosen such that the rms of the forcing field $\langle|\delta \boldsymbol{v}|^2\rangle^{1/2} = f_T V_{\rm rms}$, where $f_T = 1/n$ is the prefactor due to the n times updates per Eddy turnover timescale. A Helmholtz decomposition is done by applying the projection tensor $\boldsymbol{P}$, for which each component is given by Federrath et al. (2010),

$$\boldsymbol{P}_{ij}(\boldsymbol{k}) = \zeta \delta_{ij} + (1 - 2\zeta)\frac{k_i k_j}{|k|^2}, \tag{43}$$

where δ_{ij} is the Kronecker delta and ζ is the forcing parameter ($\zeta = 1$ for purely solenoidal and $\zeta = 0$ for purely compressive). The white-noise field is newly generated during each forcing update. Thus, this method generates forcing fields that are completely independent in time. Every turbulent perturbation is independent of previous time steps. The resulting velocity dispersion of the turbulent flow is then measured directly from the simulation output.

To test the forcing algorithm, we ran a 256^3 uniform grid hydrodynamical simulation of supersonic isothermal turbulence in a periodic box of size 5 pc on a side. The simulation was run for five turnover times $5T$, and the outputs were recorded every $0.1T$ interval. Figure 16 shows the map of projected column densities, which are visually in agreement with the known morphology of turbulent density fluctuations (e.g., Federrath et al. 2010). For a more quantitative test, the volume-weighted PDF of densities $P_V(s)$ averaged over all snapshots at $t > 1T$ (red line) is shown in Figure 17. The lognormal PDF fits very well to the simulated distribution. Although some deviations are found at both the low- and high-density tails of the distribution, such deviations are known in previous studies.
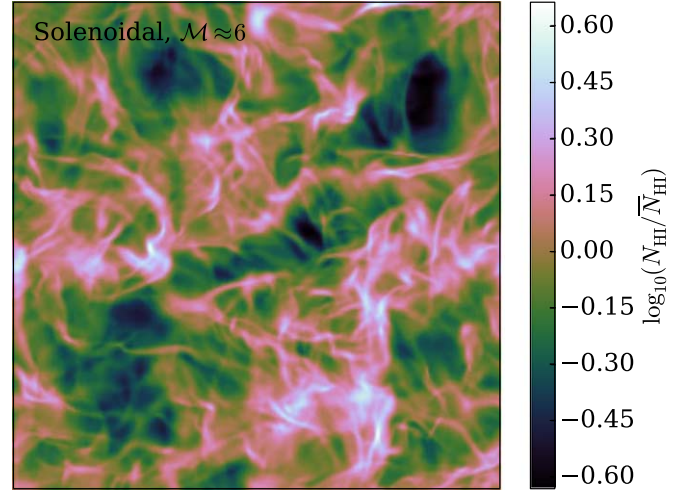

Figure 16. Map of H I column density fluctuations in a driven isothermal turbulence simulation of $\mathcal{M} \approx 6$ flow. The 256^3 simulation is with solenoidal forcing, and the box size is 5 pc on a side.
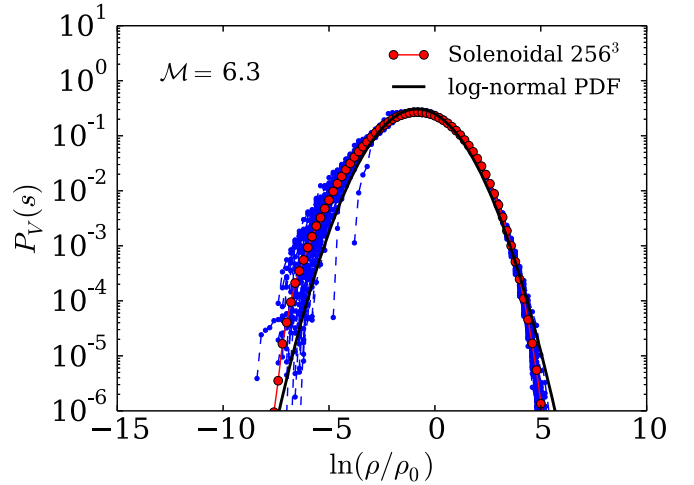

Figure 17. Volume-weighted PDF of gas density contrasts. The average PDF after $>1T$ is indicated by the red line, and the PDF of each snapshot is shown in blue. The lognormal PDF is indicated by the black line.

The departure from the lognormal PDF is likely due to the limited spatial resolution at the high-density tail and the intermittency at the low-density tail, which increases for higher Mach numbers.

Overall, our forcing algorithm in RAMSES-RT agrees with the known results of turbulence properties. We have repeated the test with 128^3 grid resolution and found an almost identical result. For the RHD turbulence simulation, we therefore adopt 128^3 resolution throughout the paper.

We also tested the convergence of the escape fraction in our fiducial RHD setup. We have repeated the simulation with 256^3 grid resolution. Figure 18 shows the comparison of the time evolution of the escape fractions in the 128^3 and 256^3 runs. The result agrees reasonably well. While the 256^3 run exhibits more fluctuations at early times, this can be understood in terms of more low-density tails in the density PDF, which allows the ionizing photons to escape before the breakout. Overall, our results should be robust against the spatial resolution of the simulations.
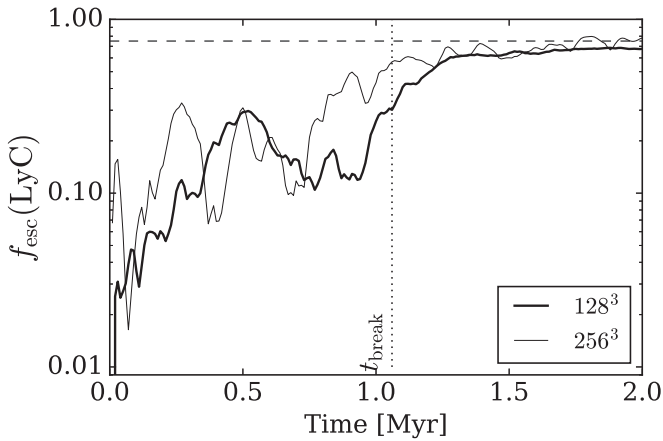
Figure 18. Convergence test of the escape fractions in the fiducial RHD simulations with two different resolutions, 128^3 (thick line) and 256^3 (thin line).

Appendix B
HST/COS Sample

In order to compare the simulation with the HST/COS observation of low-redshift LyC-leaking galaxies, we have retrieved the reduced COS G160M spectra of the $z \sim 0.3$ Izotov et al. (2016, 2018a, 2018b) sample from the MAST archive (GO 14635, PI: Izotov; GO 13744, PI: Thuan). For the measurement of LyC escape fractions and Lyα peak separations, we have used the reported values from Izotov et al. (2016, 2018a, 2018b) and Verhamme et al. (2017), which are tabulated in Table 2. For the red peak asymmetry parameter A_f, we have measured the quantity directly from the archival COS spectra after binning to the resolution matched to $R = 15,000$. We first identified the wavelengths of the red and blue peaks, $\lambda_{\rm peak}^{\rm red}$ and $\lambda_{\rm peak}^{\rm blue}$, from the maximum of each component. The valley is located at the minimum between the two peaks, corresponding to wavelength $\lambda_{\rm valley}$. The red peak asymmetry parameter is then computed as the ratio of the right-to-left flux of the red peak, $A_f = \int_{\lambda_{\rm peak}^{\rm red}}^{\lambda_{\rm max}} f_\lambda \, d\lambda \Big/ \int_{\lambda_{\rm valley}}^{\lambda_{\rm peak}^{\rm red}} f_\lambda \, d\lambda$, where $\lambda_{\rm max}$ is the maximum wavelength for the red peak, which is chosen to be $\lambda_{\rm max} = 1220$ Å. The asymmetry parameters for all objects are shown in Table 2. We use these tabulated values for our comparison with the simulation.

Table 2
HST/COS LyC-leaking Sample at $z \sim 0.3$

Name	$f_{\rm esc}^{\rm LyC}$ (%)	$\Delta v_{\rm peak}$ (km s^{-1})	A_f
J0901+2119	2.7 ± 0.7[a]	345.0 ± 12.5[a]	2.09 ± 0.19
J1011+1947	11.4 ± 1.8[a]	276.4 ± 5.4[a]	2.31 ± 0.30
J1243+4646	72.6 ± 9.7[a]	143.4 ± 4.0[a]	3.31 ± 0.45
J1248+4259	2.2 ± 0.7[a]	283.8 ± 15.9[a]	4.27 ± 0.65
J1256+4509	38.0 ± 5.7[a]	239.4 ± 10.5[a]	1.61 ± 0.24
J1154+2443	46.0 ± 2.0[b]	199.0 ± 10.0[b,e]	2.79 ± 0.31
J0925+1403	7.20 ± 0.8[c]	310.0 ± 10.0[d,e]	3.44 ± 0.46
J1152+3400	13.2 ± 1.1[c]	270.0 ± 10.0[d,e]	4.01 ± 0.54
J1333+6246	5.60 ± 1.5[c]	390.0 ± 10.0[d,e]	1.51 ± 0.20
J1442−0209	7.40 ± 1.0[c]	310.0 ± 10.0[d,e]	2.28 ± 0.10
J1503+3644	5.80 ± 0.6[c]	430.0 ± 10.0[d,e]	2.36 ± 0.34

Notes.
[a] Izotov et al. (2018b).
[b] Izotov et al. (2018a).
[c] Izotov et al. (2016).
[d] Verhamme et al. (2017).
[e] When the error in the peak separation is not explicitly stated, the ±10 km s^{-1} uncertainty corresponding to the COS spectral resolution $R = 15,000$ is used.

ORCID iDs

Koki Kakiichi ⓘ https://orcid.org/0000-0001-6874-1321
Max Gronke ⓘ https://orcid.org/0000-0003-2491-060X

References

Adams, T. F. 1972, ApJ, 174, 439
Arthur, S. J., Henney, W. J., Mellema, G., de Colle, F., & Vázquez-Semadeni, E. 2011, MNRAS, 414, 1747
Astropy Collaboration, Price-Whelan, A. M., Sipőcz, B. M., et al. 2018, AJ, 156, 123
Astropy Collaboration, Robitaille, T. P., Tollerud, E. J., et al. 2013, A&A, 558, A33
Barger, K. A., Haffner, L. M., & Bland-Hawthorn, J. 2013, ApJ, 771, 132
Bassett, R., Ryan-Weber, E. V., Cooke, J., et al. 2019, MNRAS, 483, 5223
Becker, G. D., Davies, F. B., Furlanetto, S. R., et al. 2018, ApJ, 863, 92
Benson, A., Venkatesan, A., & Shull, J. M. 2013, ApJ, 770, 76
Bland-Hawthorn, J., & Maloney, P. R. 1999, ApJL, 510, L33
Bland-Hawthorn, J., & Maloney, P. R. 2001, ApJL, 550, L231
Borthakur, S., Heckman, T. M., Leitherer, C., & Overzier, R. A. 2014, Sci, 346, 216
Bouwens, R. J., Illingworth, G. D., Oesch, P. A., et al. 2015, ApJ, 803, 34

Brunt, C. M., Federrath, C., & Price, D. J. 2010a, MNRAS, 405, L56
Brunt, C. M., Federrath, C., & Price, D. J. 2010b, MNRAS, 403, 1507
Chen, H.-W., Prochaska, J. X., & Gnedin, N. Y. 2007, ApJL, 667, L125
Chisholm, J., Gazagnes, S., Schaerer, D., et al. 2018, A&A, 616, A30
Chisholm, J., Orlitová, I., Schaerer, D., et al. 2017, A&A, 605, A67
Chung, A. S., Dijkstra, M., Ciardi, B., & Gronke, M. 2016, MNRAS, 455, 884
Crowther, P. A., Castro, N., Evans, C. J., et al. 2017, Msngr, 170, 40
Dale, J. E., Ercolano, B., & Bonnell, I. A. 2012, MNRAS, 424, 377
Dijkstra, M. 2017, arXiv:1704.03416
Dijkstra, M., Gronke, M., & Sobral, D. 2016a, ApJ, 823, 74
Dijkstra, M., Gronke, M., & Venkatesan, A. 2016b, ApJ, 828, 71
Dijkstra, M., Haiman, Z., & Spaans, M. 2006, ApJ, 649, 14
Dijkstra, M., & Loeb, A. 2008, MNRAS, 391, 457
Dijkstra, M., & Loeb, A. 2009, MNRAS, 396, 377
Doran, E. I., Crowther, P. A., de Koter, A., et al. 2013, A&A, 558, A134
Dove, J. B., & Shull, J. M. 1994, ApJ, 430, 222
Eide, M. B., Gronke, M., Dijkstra, M., & Hayes, M. 2018, ApJ, 856, 156
Eldridge, J. J., Stanway, E. R., Xiao, L., et al. 2017, PASA, 34, e058
Elmegreen, B. G., & Burkert, A. 2010, ApJ, 712, 294
Faisst, A. L. 2016, ApJ, 829, 99
Federrath, C. 2013, MNRAS, 436, 1245
Federrath, C., & Klessen, R. S. 2012, ApJ, 761, 156
Federrath, C., Roman-Duval, J., Klessen, R. S., Schmidt, W., & Mac Low, M.-M. 2010, A&A, 512, A81
Fletcher, T. J., Robertson, B. E., Nakajima, K., et al. 2019, ApJ, 878, 87
Fynbo, J. P. U., Jakobsson, P., Prochaska, J. X., et al. 2009, ApJS, 185, 526
Gazagnes, S., Chisholm, J., Schaerer, D., et al. 2018, A&A, 616, A29
Geen, S., Hennebelle, P., Tremblin, P., & Rosdahl, J. 2015, MNRAS, 454, 4484
Geen, S., Hennebelle, P., Tremblin, P., & Rosdahl, J. 2016, MNRAS, 463, 3129
Gnedin, N. Y. 2016, ApJ, 821, 50
Gnedin, N. Y., Kravtsov, A. V., & Chen, H.-W. 2008, ApJ, 672, 765
Goldbaum, N. J., Krumholz, M. R., Matzner, C. D., & McKee, C. F. 2011, ApJ, 738, 101
Gray, W. J., & Scannapieco, E. 2017, ApJ, 849, 132
Gritschneder, M., Burkert, A., Naab, T., & Walch, S. 2010, ApJ, 723, 971
Gritschneder, M., Naab, T., Walch, S., Burkert, A., & Heitsch, F. 2009, ApJL, 694, L26
Gronke, M., Bull, P., & Dijkstra, M. 2015, ApJ, 812, 123
Gronke, M., & Dijkstra, M. 2014, MNRAS, 444, 1095
Gronke, M., Dijkstra, M., McCourt, M., & Oh, S. P. 2016, ApJL, 833, L26
Gronke, M., Dijkstra, M., McCourt, M., & Peng, O. S. 2017, A&A, 607, A71
Gronke, M., Girichidis, P., Naab, T., & Walch, S. 2018, ApJ, 862, L7
Haardt, F., & Madau, P. 2001, in Rencontres de Moriond 36, Clusters of Galaxies and the High Redshift Universe Observed in X-rays, ed. D. M. Neumann & J. T. V. Tran, 64
Hansen, M., & Oh, S. P. 2006, MNRAS, 367, 979
Harikane, Y., Ouchi, M., Shibuya, T., et al. 2018, ApJ, 859, 84
Hayes, M., Östlin, G., Duval, F., et al. 2014, ApJ, 782, 6
Heckman, T. M., Borthakur, S., Overzier, R., et al. 2011, ApJ, 730, 5
Henry, A., Scarlata, C., Martin, C. L., & Erb, D. 2015, ApJ, 809, 19
Hopkins, P. F. 2013, MNRAS, 430, 1880
Hosokawa, T., & Inutsuka, S.-i. 2006, ApJ, 646, 240
Howard, C., Pudritz, R., & Klessen, R. 2017, ApJ, 834, 40
Howard, C. S., Pudritz, R. E., Harris, W. E., & Klessen, R. S. 2018, MNRAS, 475, 3121
Hummels, C. B., Smith, B. D., Hopkins, P. F., et al. 2019, ApJ, 882, 156
Imara, N., & Faesi, C. M. 2018, arXiv:1812.02180
Inoue, A. K. 2011, MNRAS, 415, 2920
Izotov, Y. I., Guseva, N. G., & Thuan, T. X. 2011, ApJ, 728, 161
Izotov, Y. I., Schaerer, D., Thuan, T. X., et al. 2016, MNRAS, 461, 3683
Izotov, Y. I., Schaerer, D., Worseck, G., et al. 2018a, MNRAS, 474, 4514
Izotov, Y. I., Worseck, G., Schaerer, D., et al. 2018b, MNRAS, 478, 4851
Jacquet, E., & Krumholz, M. R. 2011, ApJ, 730, 116
Jaskot, A. E., & Oey, M. S. 2014, ApJL, 791, L19
Jaskot, A. E., Oey, M. S., Scarlata, C., & Dowd, T. 2017, ApJL, 851, L9
Jiang, Y.-F., Davis, S. W., & Stone, J. M. 2013, ApJ, 763, 102
Jones, T. A., Ellis, R. S., Schenker, M. A., & Stark, D. P. 2013, ApJ, 779, 52
Kakiichi, K., & Dijkstra, M. 2018, MNRAS, 480, 5140
Kakiichi, K., Ellis, R. S., Laporte, N., et al. 2018, MNRAS, 479, 43
Katz, H., Galligan, T. P., Kimm, T., et al. 2019, MNRAS, 487, 5902
Kennicutt, R. C., & Evans, N. J. 2012, ARA&A, 50, 531
Kepley, A. A., Leroy, A. K., Johnson, K. E., Sandstrom, K., & Chen, C.-H. R. 2016, ApJ, 828, 50
Khaire, V., Walther, M., Hennawi, J. F., et al. 2019, MNRAS, 486, 769

Kim, J.-G., Kim, W.-T., & Ostriker, E. C. 2016, ApJ, 819, 137
Kim, J.-G., Kim, W.-T., & Ostriker, E. C. 2018, ApJ, 859, 68
Kimm, T., Blaizot, J., Garel, T., et al. 2019, arXiv:1901.05990
Kimm, T., & Cen, R. 2014, ApJ, 788, 121
Kimm, T., Haehnelt, M., Blaizot, J., et al. 2018, MNRAS, 475, 4617
Konstandin, L., Girichidis, P., Federrath, C., & Klessen, R. S. 2012, ApJ, 761, 149
Kritsuk, A. G., Norman, M. L., Padoan, P., & Wagner, R. 2007, ApJ, 665, 416
Krumholz, M. R. 2014, PhR, 539, 49
Krumholz, M. R., & Burkhart, B. 2016, MNRAS, 458, 1671
Krumholz, M. R., Klein, R. I., & McKee, C. F. 2012, ApJ, 754, 71
Krumholz, M. R., Matzner, C. D., & McKee, C. F. 2006, ApJ, 653, 361
Krumholz, M. R., & McKee, C. F. 2005, ApJ, 630, 250
Krumholz, M. R., Stone, J. M., & Gardiner, T. A. 2007, ApJ, 671, 518
Laursen, P., Sommer-Larsen, J., & Andersen, A. C. 2009, ApJ, 704, 1640
Leethochawalit, N., Jones, T. A., Ellis, R. S., Stark, D. P., & Zitrin, A. 2016, ApJ, 831, 152
Leroy, A. K., Bolatto, A. D., Ostriker, E. C., et al. 2015, ApJ, 801, 25
Lopez, L. A., Krumholz, M. R., Bolatto, A. D., et al. 2014, ApJ, 795, 121
Lopez, L. A., Krumholz, M. R., Bolatto, A. D., Prochaska, J. X., & Ramirez-Ruiz, E. 2011, ApJ, 731, 91
Ma, X., Hopkins, P. F., Kasen, D., et al. 2016, MNRAS, 459, 3614
Ma, X., Kasen, D., Hopkins, P. F., et al. 2015, MNRAS, 453, 960
Marchi, F., Pentericci, L., Guaita, L., et al. 2017, A&A, 601, A73
Marchi, F., Pentericci, L., Guaita, L., et al. 2018, A&A, 614, A11
Mas-Ribas, L., Hennawi, J. F., Dijkstra, M., et al. 2017, ApJ, 846, 11
Matthee, J., Sobral, D., Best, P., et al. 2017, MNRAS, 465, 3637
McKee, C. F., & Ostriker, E. C. 2007, ARA&A, 45, 565
McKinney, J. H., Jaskot, A. E., Oey, M. S., et al. 2019, ApJ, 874, 52
McLeod, A. F., Dale, J. E., Evans, C. J., et al. 2019, MNRAS, 486, 5263
Mellema, G., Arthur, S. J., Henney, W. J., Iliev, I. T., & Shapiro, P. R. 2006, ApJ, 647, 397
Menacho, V., Östlin, G., Bik, A., et al. 2019, MNRAS, 487, 3183
Meyer, R. A., Bosman, S. E. I., Kakiichi, K., & Ellis, R. S. 2019, MNRAS, 483, 19
Mihalas, D. 1978, Stellar Atmospheres (2nd ed.; San Francisco, CA: Freeman)
Miura, R. E., Espada, D., Hirota, A., et al. 2018, ApJ, 864, 120
Naidu, R. P., Forrest, B., Oesch, P. A., Tran, K.-V. H., & Holden, B. P. 2018, MNRAS, 478, 791
Nakajima, K., Ellis, R. S., Iwata, I., et al. 2016, ApJL, 831, L9
Neufeld, D. A. 1990, ApJ, 350, 216
Neufeld, D. A., & McKee, C. F. 1988, ApJL, 331, L87
Oesch, P. A., Bouwens, R. J., Illingworth, G. D., Labbé, I., & Stefanon, M. 2018, ApJ, 855, 105
Orlitová, I., Verhamme, A., Henry, A., et al. 2018, A&A, 616, A60
Osterbrock, D. E. 1962, ApJ, 135, 195
Östlin, G., Hayes, M., Duval, F., et al. 2014, ApJ, 797, 11
Ouchi, M., Harikane, Y., Shibuya, T., et al. 2018, PASJ, 70, S13
Owocki, S. P. 2015, in Very Massive Stars in the Local Universe, ed. J. S. Vink (Cham: Springer), 113
Paardekooper, J.-P., Khochfar, S., & Dalla Vecchia, C. 2015, MNRAS, 451, 2544
Pagel, B. E. J. 2003, in ASP Conf. Ser. 304, CNO in the Universe, ed. C. Charbonnel, D. Schaerer, & G. Meynet (San Francisco, CA: ASP), 187
Pardy, S. A., Cannon, J. M., Östlin, G., et al. 2014, ApJ, 794, 101
Pardy, S. A., Cannon, J. M., Östlin, G., Hayes, M., & Bergvall, N. 2016, AJ, 152, 178
Park, K., Ricotti, M., di Matteo, T., & Reynolds, C. S. 2014, MNRAS, 437, 2856
Pawlik, A. H., Rahmati, A., Schaye, J., Jeon, M., & Dalla Vecchia, C. 2017, MNRAS, 466, 960
Pawlik, A. H., Schaye, J., & Dalla Vecchia, C. 2015, MNRAS, 451, 1586
Pellegrini, E. W., Oey, M. S., Winkler, P. F., et al. 2012, ApJ, 755, 40
Planck Collaboration, Aghanim, N., Akrami, Y., et al. 2020, A&A, 641, A6
Pontzen, A., Roškar, R., Stinson, G. S., et al. 2013, pynbody: Astrophysics Simulation Analysis for Python, Astrophysics Source Code Library, ascl:1305.002
Prochaska, J. X., Chen, H.-W., & Bloom, J. S. 2006, ApJ, 648, 95
Puschnig, J., Hayes, M., Östlin, G., et al. 2017, MNRAS, 469, 3252
Reddy, N. A., Steidel, C. C., Pettini, M., Bogosavljević, M., & Shapley, A. E. 2016, ApJ, 828, 108
Rémy-Ruyer, A., Madden, S. C., Galliano, F., et al. 2014, A&A, 563, A31
Rhoads, J. E., Dey, A., Malhotra, S., et al. 2003, AJ, 125, 1006
Robertson, B., & Goldreich, P. 2012, ApJL, 750, L31
Robertson, B., & Goldreich, P. 2018, ApJ, 854, 88

Robertson, B. E., Ellis, R. S., Furlanetto, S. R., & Dunlop, J. S. 2015, ApJL, 802, L19
Rogers, H., & Pittard, J. M. 2013, MNRAS, 431, 1337
Rosdahl, J., Blaizot, J., Aubert, D., Stranex, T., & Teyssier, R. 2013, MNRAS, 436, 2188
Rosdahl, J., Katz, H., Blaizot, J., et al. 2018, MNRAS, 479, 994
Rosdahl, J., & Teyssier, R. 2015, MNRAS, 449, 4380
Safarzadeh, M., & Scannapieco, E. 2016, ApJL, 832, L9
Senchyna, P., Stark, D. P., Vidal-García, A., et al. 2017, MNRAS, 472, 2608
Shu, F. H. 1992, The Physics of Astrophysics, Vol. 2 (Mill Valley, CA: Univ. Science Books), 476
Shull, J. M., Moloney, J., Danforth, C. W., & Tilton, E. M. 2015, ApJ, 811, 3
Siana, B., Shapley, A. E., Kulas, K. R., et al. 2015, ApJ, 804, 17
Silant'ev, N. A., Lekht, E. E., Mendoza-Torres, J. E., & Rudnitskij, G. M. 2006, A&A, 453, 989
Smith, A., Bromm, V., & Loeb, A. 2017, MNRAS, 464, 2963
Smith, A., Ma, X., Bromm, V., et al. 2019, MNRAS, 484, 39
Smith, A., Safranek-Shrader, C., Bromm, V., & Milosavljević, M. 2015, MNRAS, 449, 4336
Steidel, C. C., Bogosavljević, M., Shapley, A. E., et al. 2018, ApJ, 869, 123
Tamura, Y., Mawatari, K., Hashimoto, T., et al. 2019, ApJ, 874, 27
Tanvir, N. R., Fynbo, J. P. U., de Ugarte Postigo, A., et al. 2019, MNRAS, 483, 5380
Teyssier, R. 2002, A&A, 385, 337
Thompson, T. A., & Krumholz, M. R. 2016, MNRAS, 455, 334
Thuan, T. X., Goehring, K. M., Hibbard, J. E., Izotov, Y. I., & Hunt, L. K. 2016, MNRAS, 463, 4268

Trebitsch, M., Blaizot, J., Rosdahl, J., Devriendt, J., & Slyz, A. 2017, MNRAS, 470, 224
Tremblin, P., Anderson, L. D., Didelon, P., et al. 2014, A&A, 568, A4
van de Voort, F., Springel, V., Mandelker, N., van den Bosch, F. C., & Pakmor, R. 2019, MNRAS, 482, L85
Vasei, K., Siana, B., Shapley, A. E., et al. 2016, ApJ, 831, 38
Verhamme, A., Orlitová, I., Schaerer, D., et al. 2017, A&A, 597, A13
Verhamme, A., Orlitová, I., Schaerer, D., & Hayes, M. 2015, A&A, 578, A7
Verhamme, A., Schaerer, D., & Maselli, A. 2006, A&A, 460, 397
Vreeswijk, P. M., Ledoux, C., Raassen, A. J. J., et al. 2013, A&A, 549, A22
Weilbacher, P. M., Monreal-Ibero, A., Verhamme, A., et al. 2018, A&A, 611, A95
Weingartner, J. C., & Draine, B. T. 2001, ApJ, 548, 296
Whalen, D., Abel, T., & Norman, M. L. 2004, ApJ, 610, 14
Whalen, D., & Norman, M. L. 2008a, ApJ, 673, 664
Whalen, D. J., & Norman, M. L. 2008b, ApJ, 672, 287
Whalen, D. J., & Norman, M. L. 2011, Ap&SS, 336, 169
Wise, J. H., Demchenko, V. G., Halicek, M. T., et al. 2014, MNRAS, 442, 2560
Wisotzki, L., Bacon, R., Brinchmann, J., et al. 2018, Natur, 562, 229
Wong, T., Hughes, A., Ott, J., et al. 2011, ApJS, 197, 16
Yajima, H., Li, Y., Zhu, Q., et al. 2014, MNRAS, 440, 776
Yang, H., Malhotra, S., Gronke, M., et al. 2016, ApJ, 820, 130
Yang, H., Malhotra, S., Gronke, M., et al. 2017, ApJ, 844, 171
Zackrisson, E., Binggeli, C., Finlator, K., et al. 2017, ApJ, 836, 78
Zackrisson, E., Inoue, A. K., & Jensen, H. 2013, ApJ, 777, 39
Zheng, Z., & Miralda-Escudé, J. 2002, ApJ, 578, 33